nks

Nordisk kernesikkerhedsforskning
Norrænar kjarnöryggisrannsóknir
Pohjoismainen ydinturvallisuustutkimus
Nordisk kjernesikkerhetsforskning
Nordisk kärnsäkerhetsforskning
Nordic nuclear safety research

NKS-249
ISBN 978-87-7893-321-8

Numerical modelling of pressure suppression pools with CFD and FEM codes

Timo Pättikangas, Jarto Niemi and Antti Timperi

VTT Technical Research Centre of Finland

June 2011

Abstract

Experiments on large-break loss-of-coolant accident for BWR is modeled with computational fluid (CFD) dynamics and finite element calculations. In the CFD calculations, the direct-contact condensation in the pressure suppression pool is studied. The heat transfer in the liquid phase is modeled with the Hughes-Duffey correlation based on the surface renewal model. The heat transfer is proportional to the square root of the turbulence kinetic energy. The condensation models are implemented with user-defined functions in the Euler-Euler two-phase model of the Fluent 12.1 CFD code.

The rapid collapse of a large steam bubble and the resulting pressure source is studied analytically and numerically. Pressure source obtained from simplified calculations is used for studying the structural effects and FSI in a realistic BWR containment. The collapse results in volume acceleration, which induces pressure loads on the pool walls. In the case of a spherical bubble, the velocity term of the volume acceleration is responsible of the largest pressure load. As the amount of air in the bubble is decreased, the peak pressure increases. However, when the water compressibility is accounted for, the finite speed of sound becomes a limiting factor.

Key words

Condensation pool, pressure suppression pool, BWR, CFD, fluid-structure interactions, FSI

NKS-249
ISBN 978-87-7893-321-8

Electronic report, June 2011

NKS Secretariat
P.O. Box 49
DK - 4000 Roskilde, Denmark

Phone +45 4677 4045
Fax +45 4677 4046
www.nks.org
e-mail nks@nks.org

RESEARCH REPORT

VTT-R-00927-11

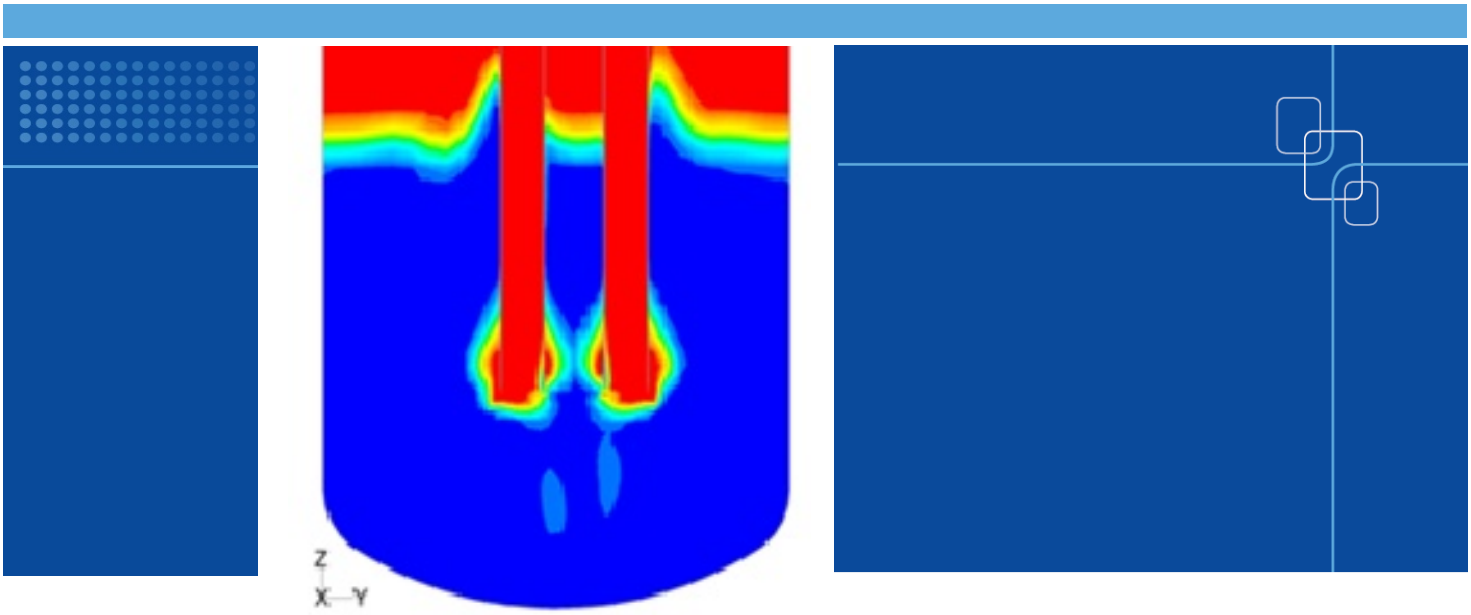

Numerical modelling of pressure suppression pools with CFD and FEM codes

Authors: Timo Pättikangas, Jarto Niemi and Antti Timperi

Confidentiality: Public

Report's title	
Numerical modelling of pressure suppression pools with CFD and FEM codes	
Customer, contact person, address	Order reference
1. Valtion ydinjäterahasto, Työ- ja elinkeinoministeriö, PL 32, 00023 VALTIONEUVOSTO 2. Nordic nuclear safety research (NKS), c/o Fortum Power and Heat Oy, Karoliina Myllymäki, PL 100, 00048 FORTUM	1. SAFIR2010 Programme: ad 9/2007SAF 2. NKS Contract no. AFT/NKS-R(10)58/7
Project name	Project number/Short name
Numerical modeling of condensation pool	41509 / NUMPOOL2010
Author(s)	Pages
Pättikangas, T., Niemi, J. and Timperi, A.	53
Keywords	Report identification code
Condensation pool, pressure suppression pool, BWR, CFD, fluid-structure interactions, FSI	VTT-R-00927-11

Summary

Experiments on large-break loss-of-coolant accident for BWR is modeled with computational fluid (CFD) dynamics and finite element calculations. In the CFD calculations, the direct-contact condensation in the pressure suppression pool is studied. The heat transfer in the liquid phase is modeled with the Hughes-Duffey correlation based on the surface renewal model. The heat transfer is proportional to the square root of the turbulence kinetic energy. The condensation models are implemented with user-defined functions in the Euler-Euler two-phase model of the Fluent 12.1 CFD code.

The rapid collapse of a large steam bubble and the resulting pressure source is studied analytically and numerically. Pressure source obtained from simplified calculations is used for studying the structural effects and FSI in a realistic BWR containment. The collapse results in volume acceleration, which induces pressure loads on the pool walls. In the case of a spherical bubble, the velocity term of the volume acceleration is responsible of the largest pressure load. As the amount of air in the bubble is decreased, the peak pressure increases. However, when the water compressibility is accounted for, the finite speed of sound becomes a limiting factor.

Confidentiality	Public

Espoo, 29.4.2011

Written by	Reviewed by	Accepted by
Timo Pättikangas, Senior Research Scientist	Mikko Manninen, Team Leader	Seppo Vuori, Customer Manager

VTT's contact address

VTT Technical Research Centre of Finland, P.O.B. 1000, FI-02044 VTT, Finland

Distribution (customer and VTT)

Karoliina Myllymäki (NKS), STUK, Timo Toppila (Fortum), Vesa Suolanen (VTT), Pavel Kudinov (KTH), Vesa Tanskanen (LUT), Markku Puustinen (LUT), Heikki Purhonen (LUT), Jani Laine (LUT), SAFIR2014 Reference Group 4

Preface

This work has been in the NUMPOOL project of the SAFIR2010 programme (The Finnish Research Programme on Nuclear Power Plant Safety). The project has been funded by Valtion ydinjäterahasto, VTT. and NKS (Nordic nuclear safety research). The authors are grateful to comments obtained from the members of the SAFIR2010 Reference Group 4 and from the Northnet Roadmap 3 Reference Group.

Espoo 24.4.2011

Authors

Contents

1 Introduction

A hypothetical large-break loss-of-coolant accident in a boiling water reactor (BWR) is being studied with the PPOOLEX experimental facility at the Lappeenranta University of Technology. PPOOLEX is a down-scaled model of a BWR containment, which has pressurized drywell and wetwell compartments (Laine et al., 2009). Vapor or air is blown to the drywell and when the pressure in the drywell increases, the gas flows through vent pipes to the water pool of the wetwell compartment. Condensation of vapor occurs via three different mechanisms. First, bulk condensation of vapor can occur both in the drywell and in the gas space of the wetwell. Second, wall condensation on the cold wall structures and on the inner walls of the vent pipes submerged in the water pool occurs. Third, direct contact condensation of vapor in the water pool occurs.

The PPOOLEX experiments have been studied with computational fluid dynamics (CFD) and finite element method (FEM) calculations. In the earlier CFD calculations, discharges of air into the drywell and to the water pool of the wetwell have been studied in detail (Pättikangas et al., 2008). The wall condensation in the drywell was also studied and the wall condensation models were improved and benchmarked against PPOOLEX experiments (Pättikangas et al., 2010a).

The direct contact condensation of vapor in the water pool was also studied in addition to the wall condensation (Pättikangas et al., 2010b). The gas flowing into the water pool contained significant amount of non-condensable gas which strongly affected the condensation process. In these studies, the CFD model was found to predict too small condensation rates compared to experiments. Therefore, better models are needed for heat transfer and interfacial area during condensation.

In the present work, direct contact condensation is studied in the PPOOLEX experiment PAR-10. Time interval after 500 seconds from the beginning of the experiment is investigated, when pure vapor is blown from the drywell into the water pool. The flow rate of vapor and the pool temperature are such that chugging is observed in the experiment: a vapor bubble is periodically forming at the vent outlet followed by rapid condensation. An attempt is made to model this process by using the so-called Hughes-Duffey model for the condensation (Hughes and Duffey, 1991).

Large, rapidly condensing steam bubbles at the blowdown pipe outlet may cause severe pressure loads on the pool structures. These loads occur usually when pure or nearly pure steam is blown into the pool water at relatively low velocity (Puustinen, 2006; Lahey and Moody, 1993). The first phase of the collapse induces a slight under-pressure on the walls. In the final phase, water velocity near the bubble increases to a high value, which creates a water-hammer propagating at the speed of sound. The possible synchronous collapse of the steam bubbles at different vent pipes would increase the loads on the pool structures.

In Section 2, the PPOOLEX experiment PAR-10 is first discussed. The Hughes-Duffey model for the heat transfer in direct-contact condensation is reviewed. The two-phase CFD model for simulations of the experiment is described. The obtained simulation results for direct contact condensation of bubbles are discussed in detail.

In Section 3, the order of accuracy of pressure wave calculations and of coupled Fluid-Structure Interaction (FSI) calculations is first studied in simplified test cases. Both CFD and

acoustic FEM models are tested for the fluid. The bubble collapse and the resulting loads are then studied analytically and numerically. Finally, the obtained pressure source is used for analyzing the structural effects in a realistic BWR containment by using the acoustic FEM model with one- and two-way FSI coupling. The Star-CD 4.08 and Abaqus 6.9-2 codes are used for the CFD and FEM calculations, respectively. The MpCCI 3.0.6 code is used for the coupled CFD-FEM calculations.

2 CFD calculations of the interaction of multiple vent pipes

In the following, the PPOOLEX experiment PAR-10 is investigated. The main focus is on the modeling of direct contact condensation in the chugging phase of the experiment. In addition, some observations on the synchronous behavior of the parallel vent pipes is made.

2.1 PPOOLEX experiment PAR-10

The PPOOLEX facility is an about 31 m^3 pressurized cylindrical vessel with a height of 7.45 meters and a diameter of 2.4 meters. The volume of the drywell compartment is 13.3 m^3 and the volume of the wetwell compartment is 17.8 m^3. Steam is blown into the drywell compartment via a horizontal DN200 (∅219.1 × 2.5 mm) inlet plenum. The experimental facility has earlier been described in detail by Puustinen, Laine and Räsänen (2010).

In 2010 experiments were performed, where the interaction of two parallel vent pipes was studied. Two DN200 (∅219.1 × 2.5 mm) vent pipes were positioned in non-axisymmetric locations. The pipes were located 300 mm and 430 mm away from the centre axis of the facility.

In the following, we study in detail the chugging phase of the experiment PAR-10 with two parallel vent pipes. In this experiment, steam blow into the drywell compartment was started at time t = 0. We concentrate on the time interval t = 500...600 s of the experiment when chugging was found to occur. The experimental parameters were fairly constant during this time interval.

The CFD calculation was carefully initialized to correspond to the situation at time t = 500 s. It was assumed that the amount of non-condensable gas in the drywell was very small because almost all air had already been blown to the wetwell. The mole fraction of air in the drywell was assumed to be 1.25 %. The temperature of the gas in the drywell was 140 °C. Since the drywell was insulated, the walls were initialized to the same temperature. The pressure in the drywell was p_{DW} = 2.89 bar.

The water level in the wetwell was at this time 2.24 m from the bottom of the pool. The submergence depth of the vent pipes was 1.15 m, which corresponds to a hydrostatic pressure of about p_{hyd} = 11.3 kPa at the level of the vent pipe outlets. The pressure in the gas space of the wetwell was initialized to $p_{WW} = p_{DW} - p_{hyd}$. In the pool, the linear hydrostatic pressure profile was initialized. The temperature of the water pool was 43 °C. The temperature of the gas space of the wetwell was stratified such that a linear temperature profile between 33 °C and 61 °C was used in the initialization. In the water pool, the wall structures were initialized to the water temperature. In the gas space, the walls were initialized to the temperature of the thermally stratified gas. The mole fraction of vapor in the gas space was assumed to be 3.2%. The wetwell compartment was uninsulated and convective heat transfer to the ambient laboratory (T = 20 °C) was used as a boundary condition.

The vent pipes were initialized to contain water below the water level of the pool. Above the water level, the vent pipes contained initially air (with a mole fraction of 3.2% of vapor). The temperature of the gas in the vent pipes was similarly stratified as in the wetwell. The initial temperature of the walls of the pipes had the same temperature as the gas or water at the corresponding level.

The mass flow rate of vapor from the inlet plenum to the drywell was 0.523 kg/s and it was kept constant during the calculation. The temperature of the vapor was 155 °C and it contained a mass fraction of 1% of air.

Let us analyze the experimental parameters by using the chugging maps presented by Lahey and Moody (1993). Assume that half of the gas blown into the drywell flows through each vent pipe. Then the average mass flow rate in a single vent pipe is 0.262 kg/s. The mass flux in a single vent pipe is then $\dot{m}'' = 7.3$ kg/m^{2}s. The mass flux together with the pool temperature (43 °C) determines the qualitative behavior of the flow through the vent pipe.

Typical regions for the condensation modes are shown in Figure 1. The experiment PAR-10 is located in the chugging region of the chart. In the chugging mode, vapor is blown out from the vent followed by a rapid condensation in the pool. Then, a water column flows back into the vent pipe and the cycle is repeated. This cycle is schematically represented in Figure 2.

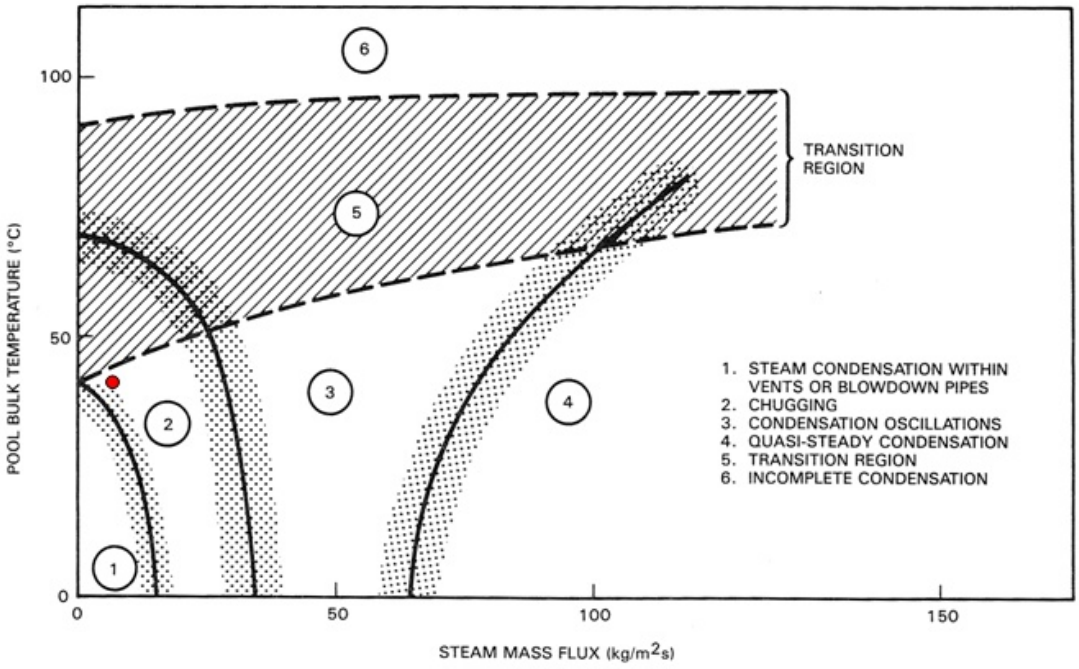

Figure 1. Typical regions for condensation modes according to Lahey and Moody (1993). The experiment PAR-10 has been marked in the map with a red dot.

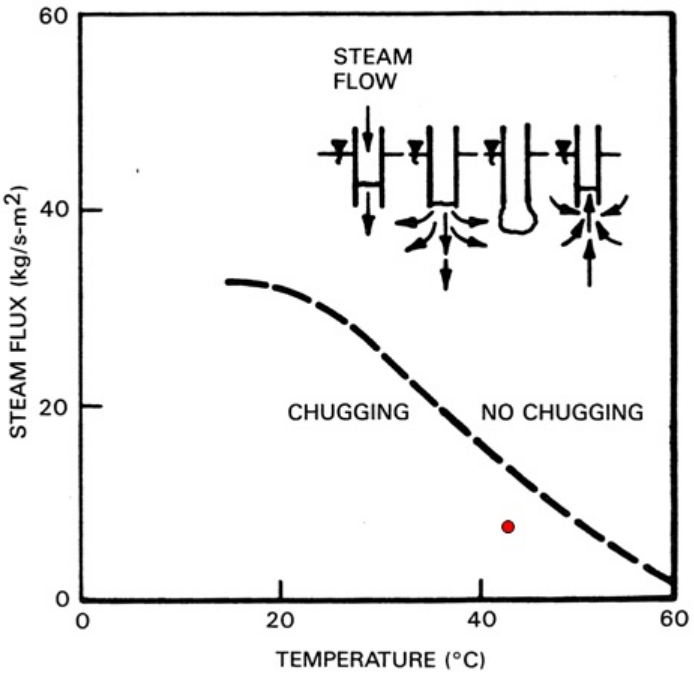

Figure 2. Sample chugging map for vertical vents according to Lahey and Moody (1993). The experiment PAR-10 has been marked in the map with a red dot.

2.2 CFD model for the experiments with two vent pipes

The surface mesh of the CFD model prepared for the PPOOLEX facility with two vent pipes is shown in Figure 3. The horizontal inlet plenum and the drywell and wetwell compartments can be seen of the left-hand side. Two vertical vent pipes from the drywell compartment to the water pool of the wetwell compartment can also be seen. Details of the floor of the drywell compartment are shown in the top frame on the right-hand side. The outlets of the vent pipes are shown in the bottom frame on the right-hand side. The fully hexahedral mesh contains about 180 000 grid cells.

The CFD calculations were performed by using the Euler-Euler two-phase model of Fluent 12.1. The Euler-Euler model is a two-fluid model, where conservation of mass, momentum and energy are solved for gas and liquid water. The gas phase consisted of two species components: dry air and vapor. The mixture of the gases was treated as a compressible ideal gas. The floating operating pressure option of Fluent was used for modeling the increasing pressure inside the vessel. The turbulence was modeled with the standard k-ε model for the mixture of the phases.

The condensation and evaporation were calculated with the previously developed model, which has been implemented in Fluent by using user-defined functions (Pättikangas et al., 2010a, 2010b). The wall structures were described with ten nodes, where one-dimensional heat conduction was solved through the wall. In wall-condensation, the heat balance on the wall surface was calculated and the condensed/evaporated mass of vapor/liquid was resolved. The water film on the wall was only taken into account with a simple model, where the film thickness was determined from the amount of liquid water in the near-wall grid cell.

The direct-contact condensation is modeled with a similar heat balance calculation as the wall condensation. The amount of condensation/evaporation is resolved from the heat balance on the liquid-vapor interface.

The heat transfer coefficient on liquid side was changed compared to previous calculations. The model of Hughes and Duffey (1991) based on the surface renewal theory of Banerjee (1978) was used with modifications introduced by Coste et al. (2008). This model has recently been used, e.g., by Štrubelj et al. (2010) and by Tanskanen (2008). In the following, the formulation of the model by Štrubelj et al. (2010) is discussed.

The heat transfer coefficient on the liquid side is

$$HTC_{\mathrm{L}} = \frac{\lambda_{\mathrm{L}} \mathrm{Nu}_{\mathrm{L}}}{L_{\mathrm{t}}} \tag{1}$$

where Nu_{L} is the Nusselt number, λ_{L} is the thermal conductivity and L_{t} is the turbulent length scale. The subscript L refers to “liquid”. The Nusselt number is

$$\mathrm{Nu}_{\mathrm{L}} = \frac{2}{\sqrt{\pi}} \mathrm{Re}_{\mathrm{t}} \, \mathrm{Pr}_{\mathrm{L}}^{1/2} \tag{2}$$

where Pr_{L} is the Prandtl number and the turbulent Reynolds number is:

$$\mathrm{Re}_{\mathrm{t}} = \frac{L_{\mathrm{t}} u_{\mathrm{t}}}{\nu_{\mathrm{L}}} \tag{3}$$

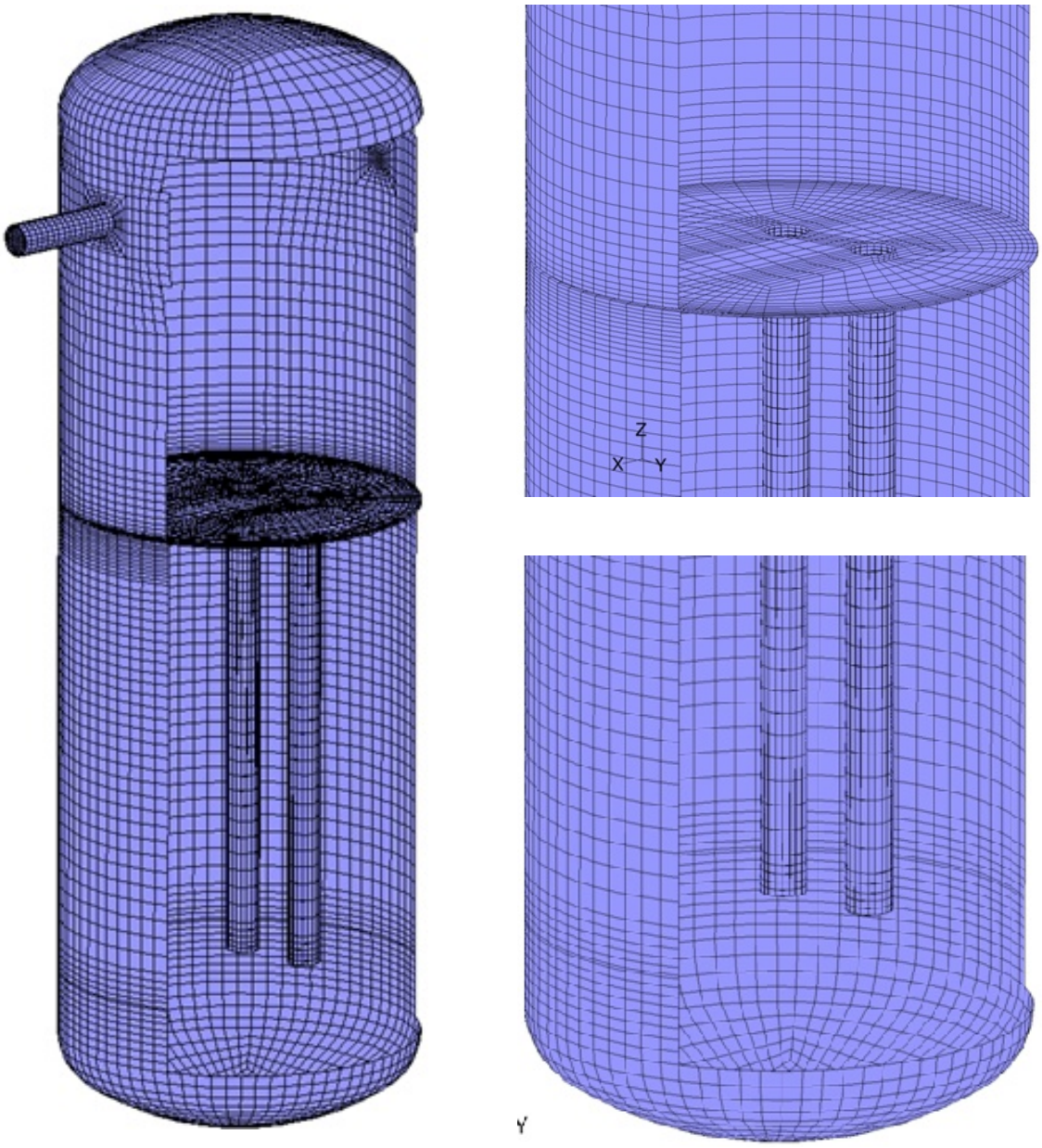

Figure 3. Surface mesh of the CFD model for experiments with two vent pipes.

The kinematic viscosity of liquid is ν_L and the turbulent velocity scale is

$$u_t = C_\mu^{1/4} k_L^{1/2} \tag{4}$$

where $C_\mu = 0.09$ and k_L is the liquid turbulence kinetic energy. The turbulent length scale is defined as

$$L_t = C_\mu \frac{k_L^{3/2}}{\varepsilon_L} \tag{5}$$

where ε_L is the turbulence dissipation.

A rough estimate for the heat transfer coefficient can be made by using the results of the CFD simulations near the outlets of the vent pipes. The turbulent length scale is of the order of $L_t \sim 1$ mm. The turbulent velocity scale is roughly $u_t \sim 1$ m/s. The turbulent Reynolds number is of the order of $\mathrm{Re}_t \sim 1000$, where $\nu_L = 10^{-6}$ m^2/s has been used. An estimate for the Nusselt number is $\mathrm{Nu}_L \sim 2500$, where $\mathrm{Pr}_L = 5$ has been assumed. The heat transfer coefficient on the liquid side is of the order $HTC_L \sim 1.5$ MW/m^{2}K, where the value $\lambda_L = 0.6$ W/mK has been used. This value is much larger than the heat transfer coefficient used in our previous simulations, where too weak direct contact condensation was obtained (see Pättikangas et al., 2010a and 2010b).

One should note, that the heat transfer coefficient actually is determined by the turbulence kinetic energy on the liquid side, which can be seen by substituting Eqs (2)–(5) into Eq. (1). The heat transfer coefficient can be rewritten as

$$HTC_L = \frac{2}{\sqrt{\pi}} C_\mu^{1/4} \frac{\lambda_L}{\nu_L} \mathrm{Pr}_L^{1/2} k_L^{1/2} \tag{6}$$

Inserting the material properties given above, one obtains

$$HTC_L = 0.83\, k_L^{1/2} \tag{7}$$

where the units are $[k_L]$ = m^2/s^2 and $[HTC_L]$ = MW/m^{2}K.

The direct contact condensation is also affected by heat transfer from the gas to the interface between gas and liquid. The interfacial heat transfer from the gas phase is, however, usually much smaller than from the liquid phase (Banerjee, 1978). The constant value of HTC_G = 1 kW/m^{2}K, which was used in our previous simulations, is also used in the present work.

The standard k-ε model for the mixture of the phases is used the following simulations. Therefore, information is only available of the turbulence kinetic energy for the mixture of the phases. This value is used as an approximation for the turbulence kinetic energy of the liquid phase that is needed in Eqs (1) and (7). Turbulence could also be modeled separately for each phase, which means that both phases would have separate values for the turbulence kinetic energy and dissipation. Such more sophisticated turbulence models are, however, numerically more unstable that the turbulence model for the mixture of the phases. Therefore, the k-ε model for the mixture of the phases was chosen.

In addition to the heat transfer coefficients, the area density between the phases affects crucially the direct contact condensation. The simple model was used, where the area density is estimated from the gradient of the volume fraction of gas, i.e., $a_i = \nabla\alpha$.

2.3 Simulation results

In the following, the results for the simulation of the experiment PAR-10 are discussed. The simulation was first initialized to the situation corresponding to the experiment at time t = 500 s as was described in Sec. 2.1. In the initialization, the vent pipes, however, contained non-condensable air above the water level and water below the water level. During first two seconds of the simulation, the water plug and the air were expelled from the vent pipe. After this, pure vapor started flowing from the vent pipes into the water pool.

In Figure 4, the mass flow rate of vapor through the vent pipes is shown. The vent pipes are periodically cleared from water and large bubbles are formed at the vent outlets, when the mass flow rate has its maximum value. Then, water flows to the vent pipe and the flow stops. The cycle is repeated and new bubbles are formed. The time interval between the bubbles is Δt = 0.55 s.

In Figure 5, the total direct contact condensation rate in the water pool for the two vent pipes is shown. The condensation rate has similar periodic form as the mass flow rate through the vent pipes. The condensation rate is, however, slightly delayed compared to the mass flow rate: the maxima of the condensation occur on the average 0.055 s later than the maxima of the mass flow rate. The condensation is strongest during the collapse phase of the bubbles at the vent outlets.

In Figure 6, the cumulative condensed mass in the water pool is compared to the cumulative mass of vapor injected into the drywell. The condensation rate can be seen to correspond accurately to the quasi stationary experimental situation, where the pressure and temperature vary only very slowly. The difference between the curves is due to the water plug and non-condensable gas that were initially in the vent pipes in the CFD simulation.

We next investigate in detail the formation and the condensation of the vapor bubbles that are formed at the vent outlets at time t = 3.5 s.

In Figure 7, the volume fraction of gas is shown in the time interval t = 3...4 s. The results are shown in the plane containing the axes of the vent pipes. At time t = 3.25 s, the mass flow rate through the vent pipes is almost zero. The direct contact condensation reaches its minimum value at time t = 3.35 s. Then, the mass flow rate is already increasing and a bubbles are formed simultaneously at both vent outlets at time t = 3.55 s. The condensation reaches its maximum value at time t = 3.60 s. Some gas starts rising upwards but vapor is completely condensed before it reaches the water level. Vapor is condensed at the vent outlets and some water flows into the vent pipes before the formation of the next bubbles starts.

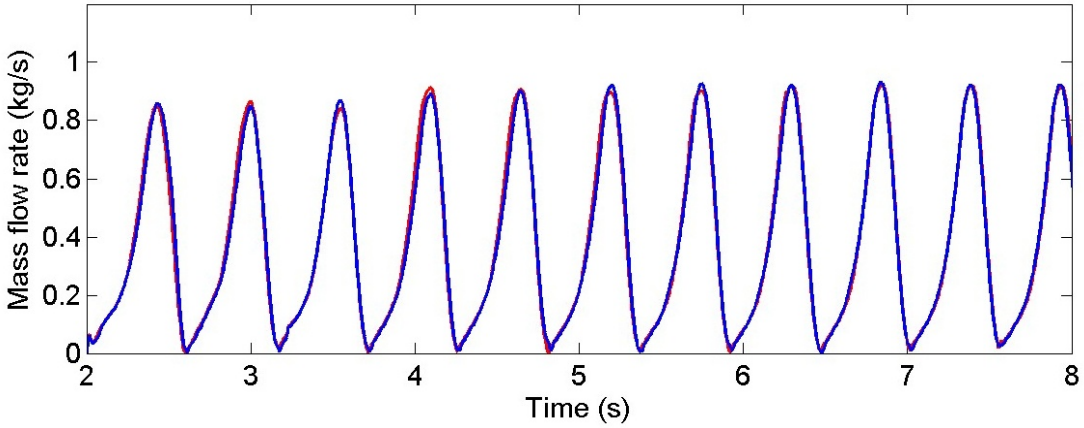

Figure 4. Mass flow rate (kg/s) through the vent pipes from the drywell to the wetwell. Results for the vent pipe 1 (red curve) and vent pipe 2 (blue curve) are shown at the monitoring location (z = 3.89 m), which is close to the roof of the wetwell (z = 4.20 m).

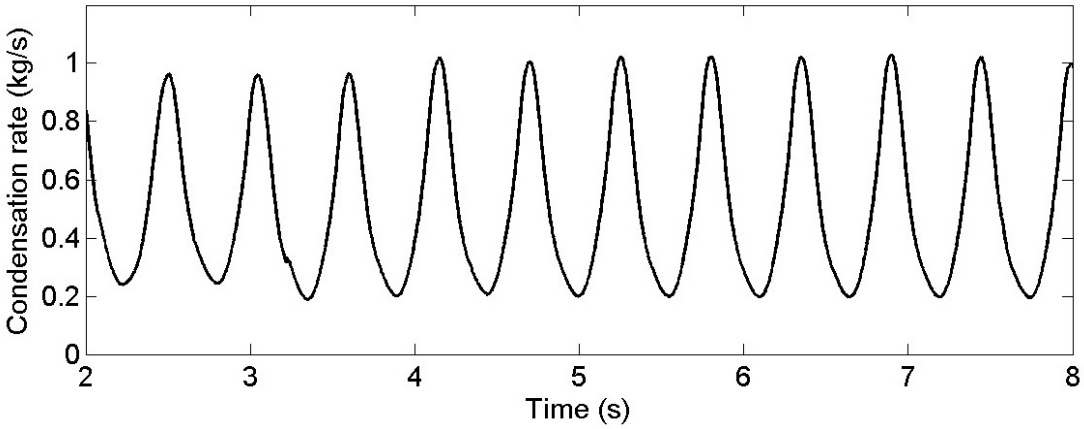

Figure 5. Direct contact condensation rate in the water pool.

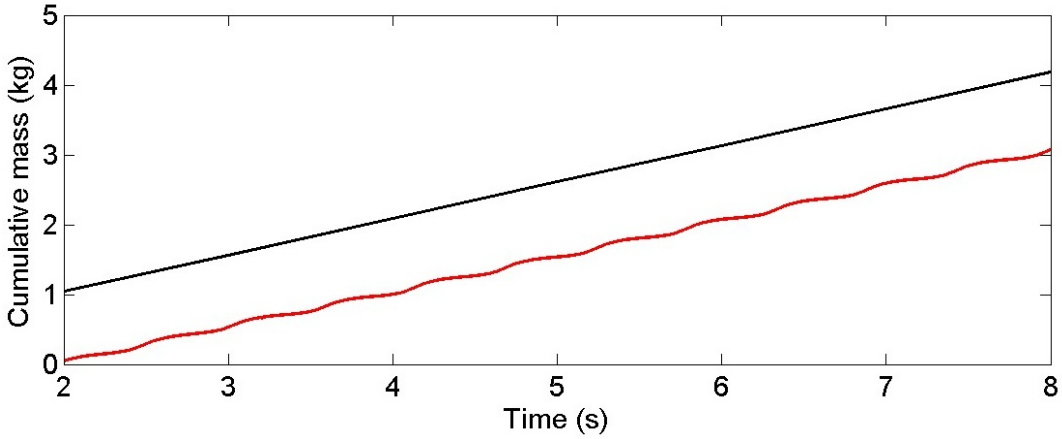

Figure 6. Cumulative condensed mass in the water pool (red curve) and cumulative mass of vapor injected into the drywell (black curve).

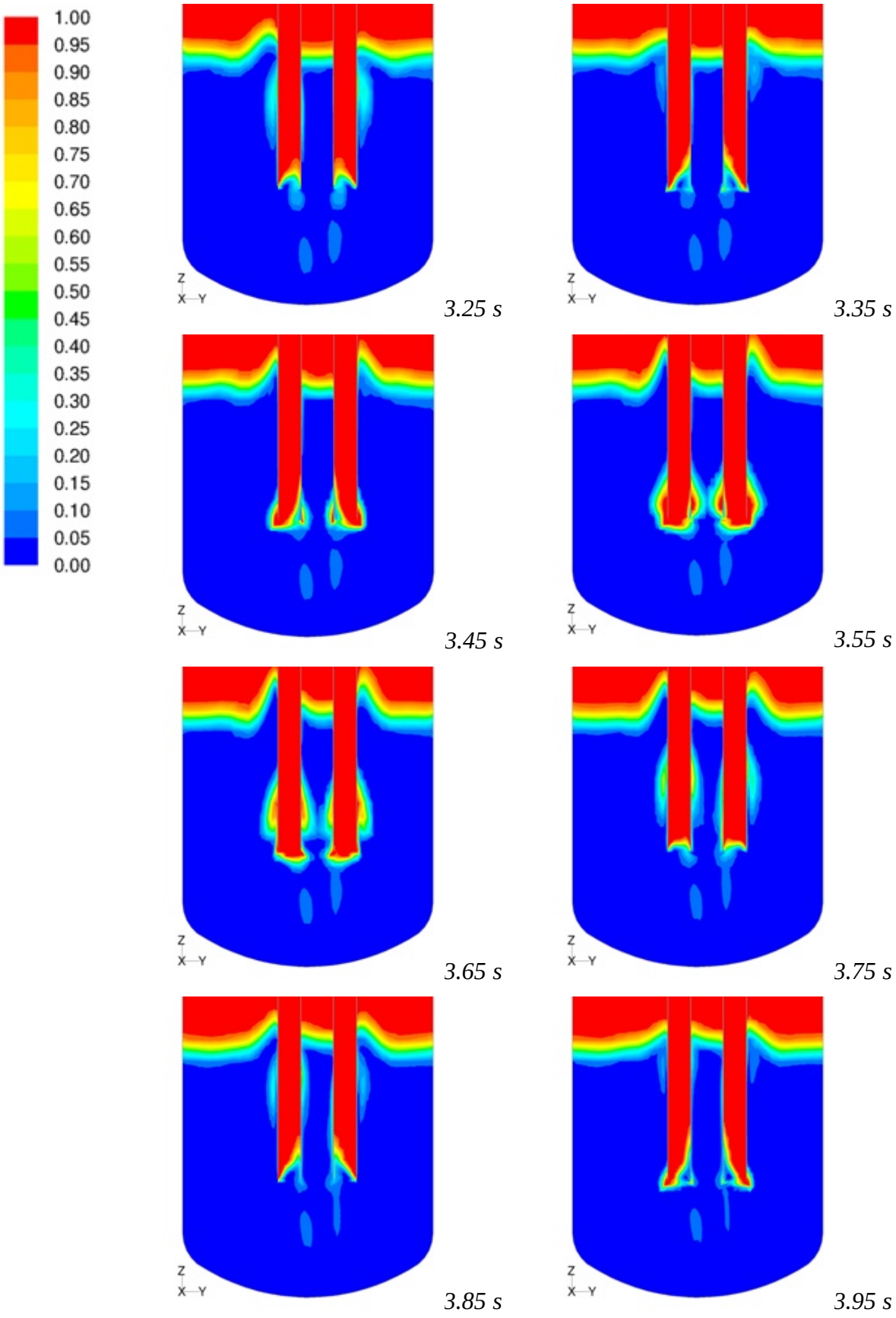

Figure 7. Volume fraction of gas at different instants of time during condensation of a gas bubble.

In Figure 8, the mole fraction of vapor is shown. In the simulation, the drywell was initialized to contain a mole fraction of 1.25 % of non-condensable air. When condensation of vapor occurs near the vent outlets, the mole fraction of the non-condensable gas increases locally. The mole fraction of non-condensable gas approaches 100% when the gas plume rises upwards. All the vapor injected into the water pool is condensed.

In Figure 9, the magnitude of the flow velocity of the gas phase is shown in a logarithmic scale. At time t = 3.25 s, the flow velocity in the vent pipes has started to increase. The velocity achieves its maximum value of about 15 m/s when the bubbles are formed at the vent outlets. After this, the flow velocity decreases rapidly and reaches its minimum value at time t = 3.72 s. Then, the flow velocity increases again and the formation of the next bubbles starts.

Figure 10 shows the heat transfer coefficient in the liquid by using a logarithmic scale. The heat transfer coefficient is calculated from the Hughes-Duffey model as was discussed in Sec. 2.2. The heat transfer coefficient achieves its minimum value approximately at time t = 3.35 s, which about 0.2 s after the minimum value of the mass flow rate occurs. The heat transfer coefficient has largest values at time t = 3.55 s, when the bubbles at the vent outlets are formed. Some large values are also seen in the regions of the rising gas plumes around the vent pipes.

Figure 11 shows the liquid generation rate from vapor in the direct contact condensation. The maximum condensation rate occurs at time t = 3.60 s, see Figure 5. At this time, the heat transfer coefficient is large and the interface area between the phases is also large. Strong condensation also occurs when water flows into the vent pipes.

The overall behavior and the amount of direct contact condensation obtained in the simulation are in agreement with the observations in experiment PAR-10. The more detailed inspection of the results revealed, however, some differences. In the experiment, chugging is found to occur. The condensation occurs near the vent outlets and no rising bubble bloom is observed. In the simulation, the condensation partly occurs in the rising bubble plume. Even though all the vapor is condensed in the simulation, it seems that the condensation rate near the vent outlets is smaller than in the experiment.

In the present simulations, the interfacial area between liquid and gas was calculated from the simple gradient model, where $a_i = \nabla\alpha$ was assumed. The behavior of the interfacial area is in the experiment more complicated. A rapid increase of the area during the bubble collapse may explain some of the differences between the simulation and the experimental observations.

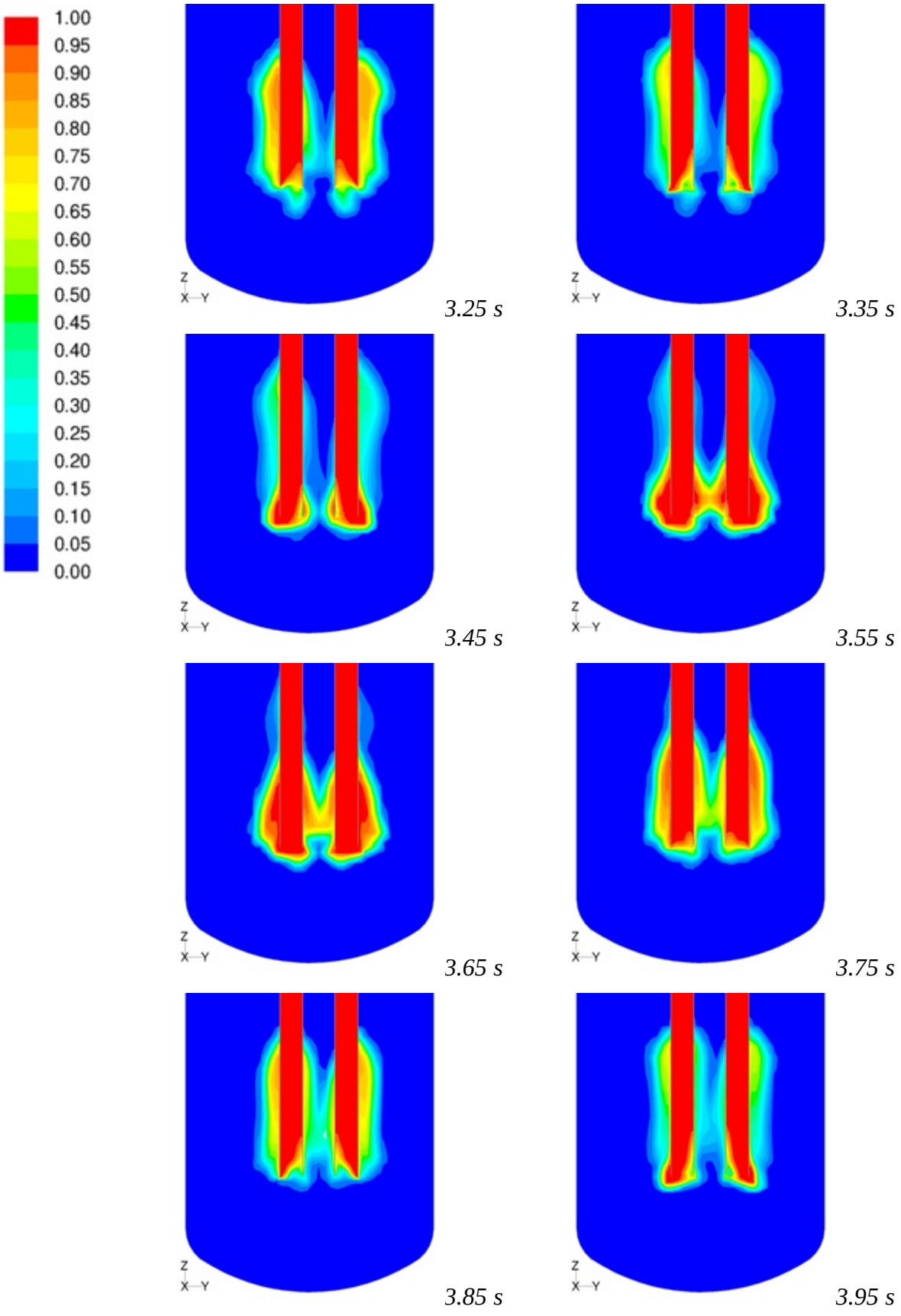

Figure 8. Mole fraction of vapor in the gas phase.

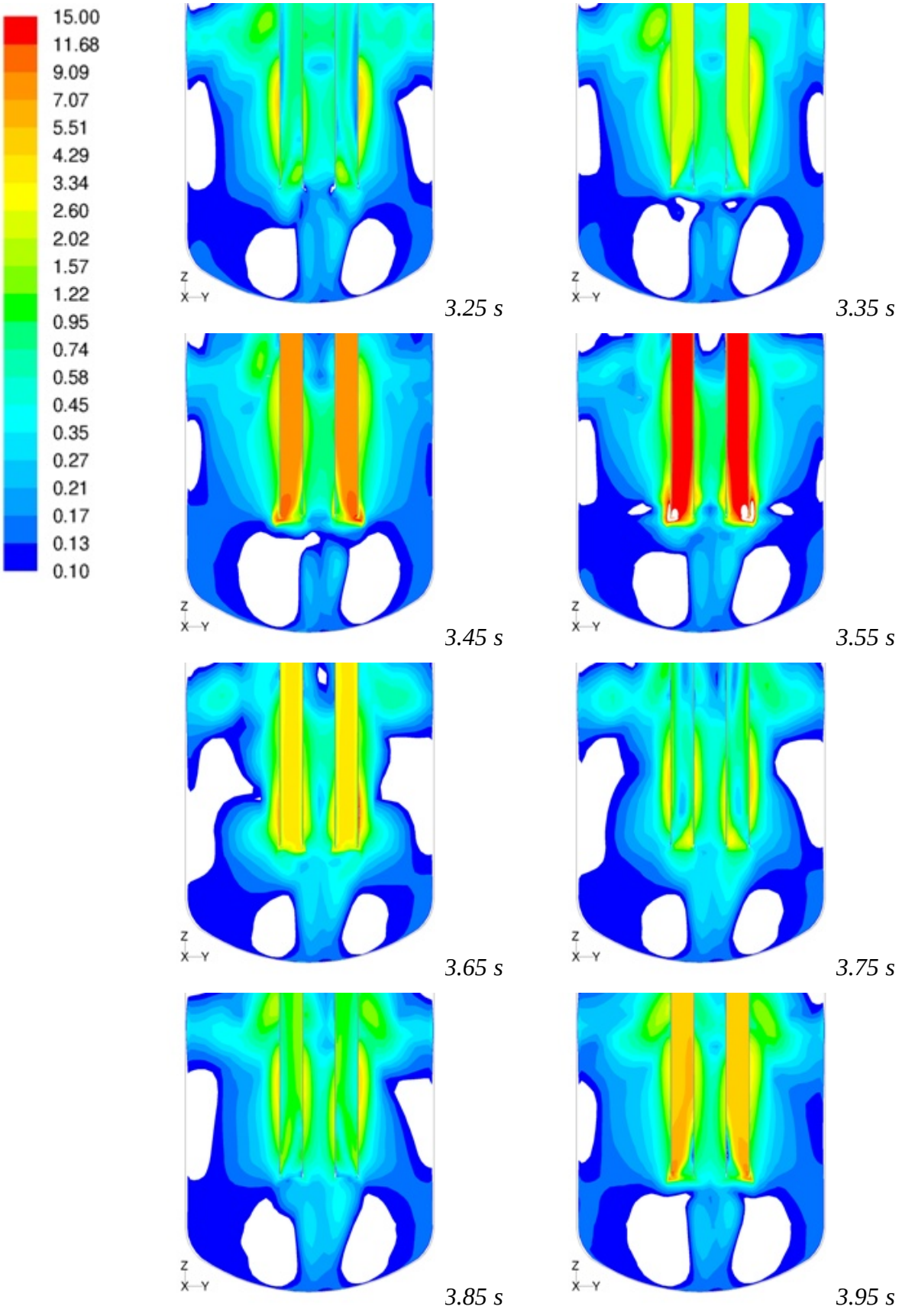

Figure 9. Magnitude of the flow velocity (m/s) of the gas phase during the condensation of a vapor bubble. Note that the scale is logarithmic.

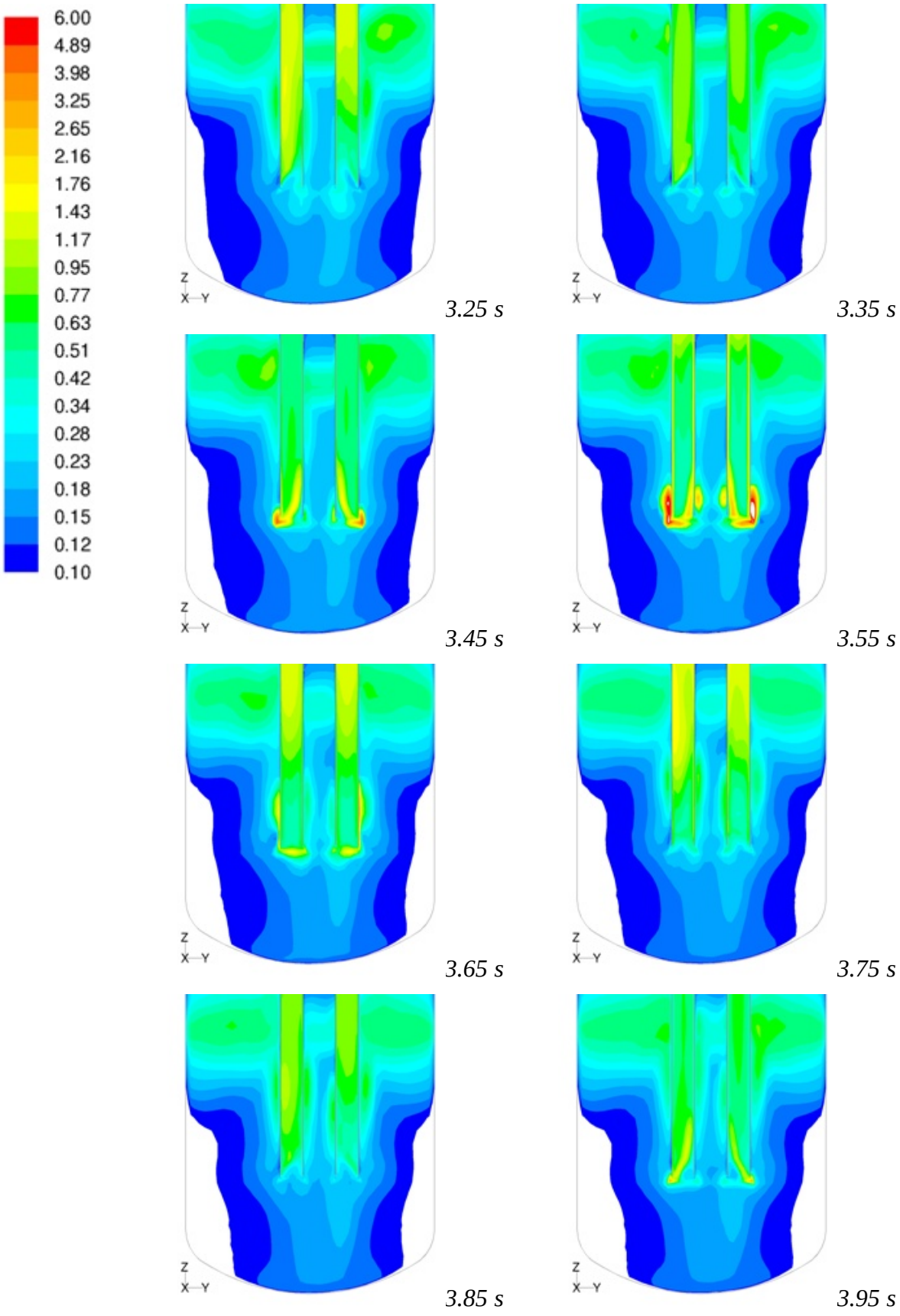

Figure 10. Heat transfer coefficient (MW/m^{2}K) on the liquid side during the condensation of a vapor bubble. Note that the scale is logarithmic.

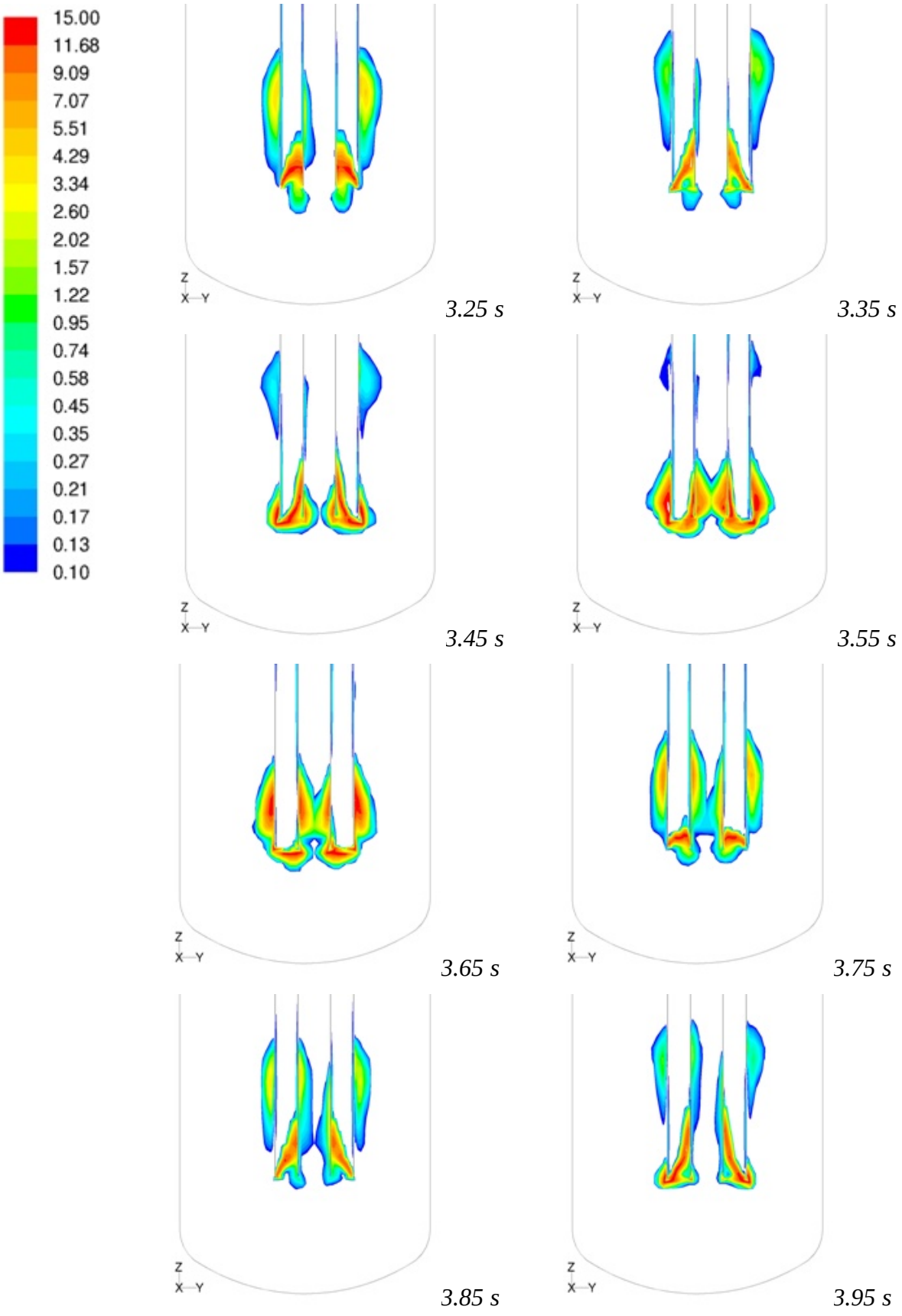

Figure 11. Mass transfer rate (kg/m^{3}s) in direct contact condensation of a vapor bubble. Note that the scale is logarithmic. Values below the indicated scale are not shown.

3 Fluid-structure interaction calculations

3.1 Order of accuracy considerations

3.1.1 Propagation of a pressure pulse

The one-dimensional problem of propagation of a sinusoidal pressure pulse was first solved by using different time steps, cell lengths and solution methods. For the fluid, density ρ_0 = 1000 kg/m^3 and speed of sound c = 1000 m/s were assumed, which correspond approximately to the values of water. In Star-CD, the following linear equation of state was used for density:

$$\rho = \rho_0 + (p - p_0)/c^2 \tag{8}$$

where the reference pressure is p_0 = 1 bar. Pressure boundary condition at the model boundary was

$$p = \begin{cases} \frac{\hat{p}}{2}\left(1 - \cos\frac{2\pi t}{\tau}\right), & 0 \le t < \tau \\ 0, & t \ge \tau \end{cases} \tag{9}$$

where τ is the duration of the pulse defined by the speed of sound and the pulse wavelength: $\tau = \lambda/c$. The wavelength was chosen as λ = 1 m so that the duration becomes τ = 1 ms. Amplitude of the pulse was chosen $\hat{p}$ = 1 bar, so that only very small density variations result. The calculated cases and parameters are shown in Tables 1 and 2 below.

Table 1. Solution methods and cell lengths used in calculating the pressure pulse.

Code	Solution method	Time discretization	Accuracy	Δx [m]
Star-CD	PISO	n.a.	1. - 2. order	0.025 / 0.05 / 0.1
	SIMPLE	3 time-level	2. order	0.05
Abaqus	FEM wave equation	Newmark	n.a.	0.05

Table 2. Calculation parameters obtained with different cell lengths and time steps.

Δx [m]	$\lambda/\Delta x$	Δt [s]	$\tau/\Delta t$	$CFL_c = c\Delta t/\Delta x$
0.025	40	5e-7 … 1e-4	10 … 2000	0.02 … 4
0.05	20	1e-6 … 1e-4	10 … 1000	0.02 … 2
0.1	10	1e-6 … 1e-4	10 … 1000	0.01 … 1

Figure 12 shows the pressure pulse after about 2.5 meters of propagation for the Star-CD PISO calculation with different time steps. The error behavior is plotted for the Star-CD calculations in Figure 13. The error is defined as the numerical damping of the peak pressure when it has arrived at the monitored location:

$$\varepsilon = \frac{\hat{p} - \hat{p}_{calc}}{\hat{p}} \qquad (10)$$

For the Star-CD calculations, the pressure was taken about 10 m from the boundary condition. Note that in the plots, the "sound speed Courant number" is defined $CFL_c = c\Delta t/\Delta x$. It is seen that the numerical damping of the pressure pulse is very strong in the Star-CD calculations unless a very short time step is used. Also the convergence rate is poor, i.e. generally clearly less than 1. order. With the shortest cell length, however, about 1. order accuracy is obtained. The accuracy is about the same for PISO and SIMPLE, although the former is clearly faster in this kind of calculation. These results are not very surprising as the pressure correction methods used are probably not designed for this kind of problem.

In Figure 14, the error behavior is plotted for the Abaqus calculations 12.5 and 25 m from the boundary condition. It is seen that the error has approximately 2. order behavior and is significantly smaller compared to the Star-CD calculations. This could be expected as the acoustic FEM calculation is intended for this kind of problem.

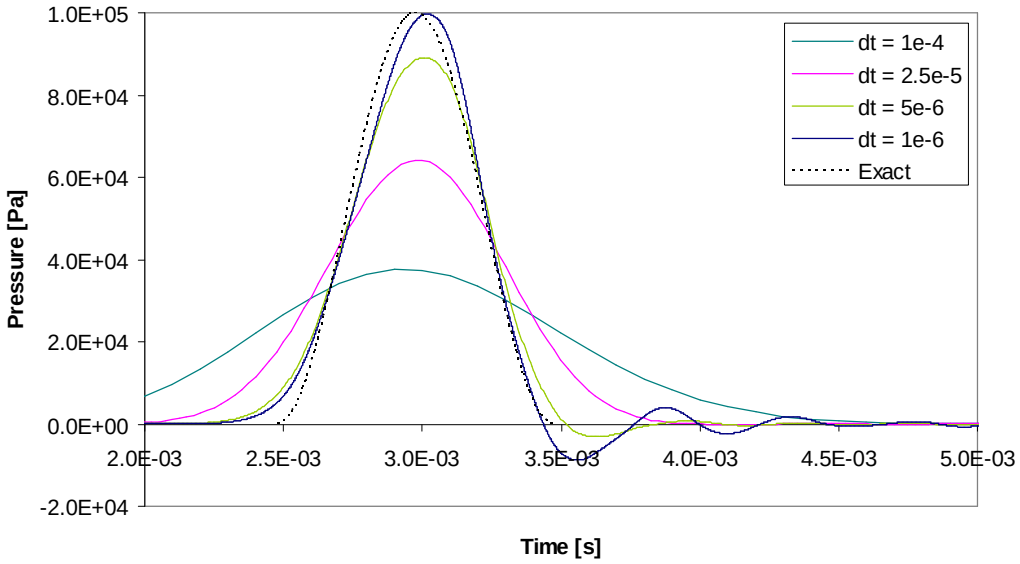

Figure 12. Pressure pulse at x = 2.5 m for PISO algorithm with Δx = 0.05 m and for exact solution.

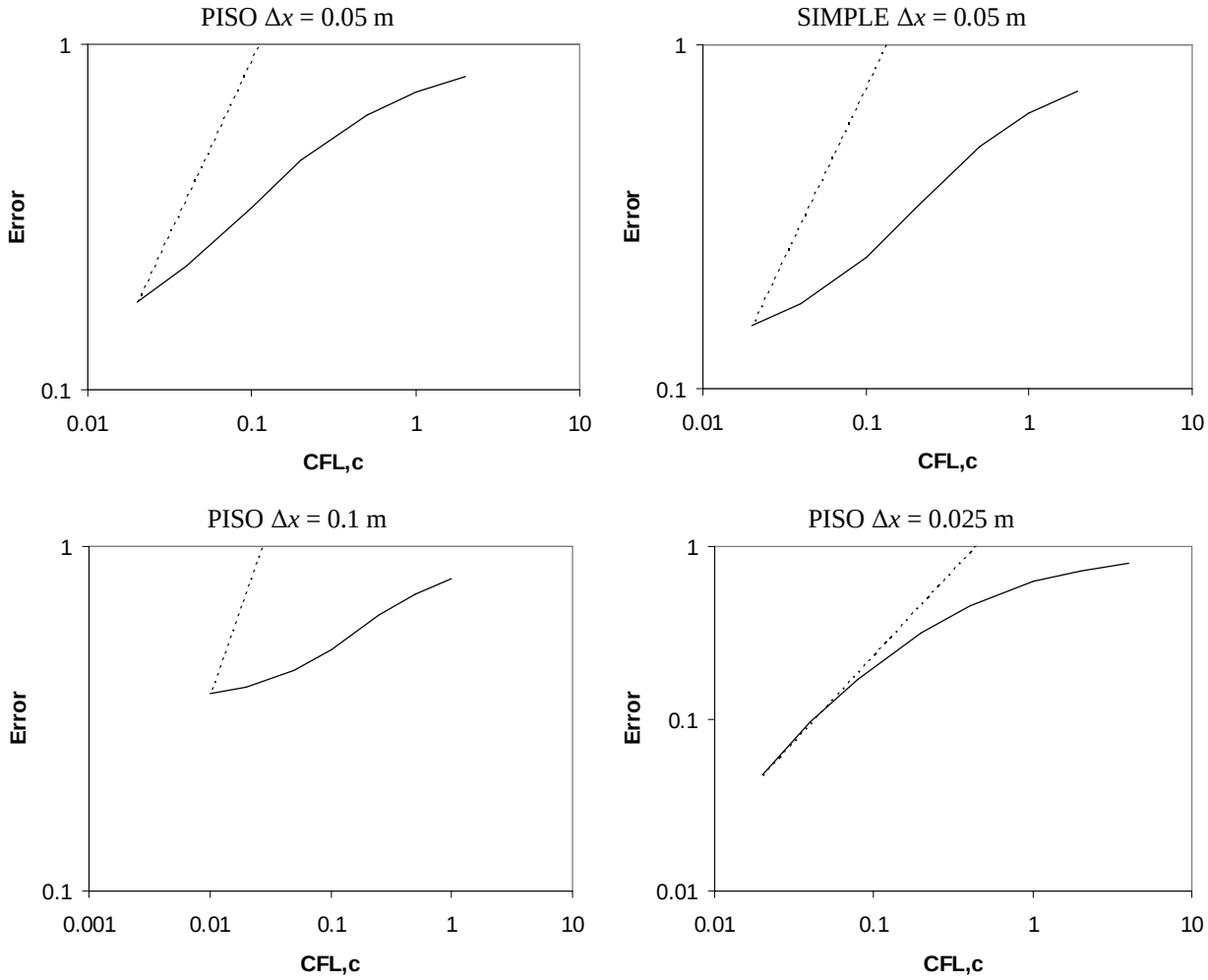

Figure 13. Reduction of error for CFD calculation of the pressure pulse at x = 10 m. First order slope is shown with dotted line.

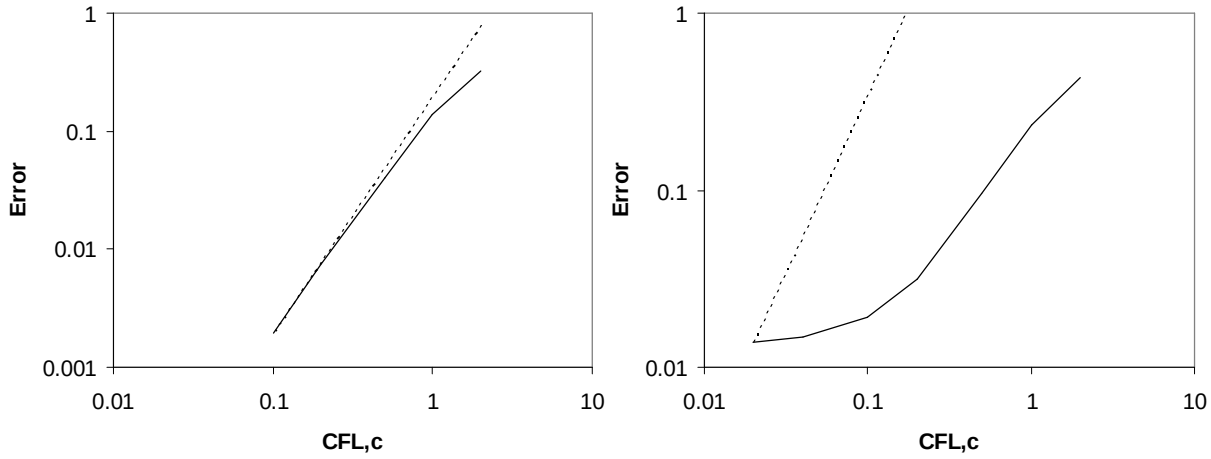

Figure 14. Reduction of error for acoustic FEM calculation of the pressure pulse at x = 12.5 m (left) and x = 25 m (right). Second order slope is shown with dotted line.

3.1.2 Oscillating mass and beam

An undamped single degree-of-freedom (d.o.f.) oscillator and a beam supported from its other end, shown in Figure 15, were used for testing the accuracy of time integration of structural problems in Abaqus. The both cases had an initial displacement (given at the tip for the beam) after which they were left free to oscillate. The beam was modeled with 10 beam elements.

For the single d.o.f. oscillator, error was calculated from the numerical damping of the oscillation amplitude after 10 cycles:

$$\varepsilon = \hat{u} - \hat{u}_{calc} \tag{11}$$

The beam was let to vibrate for about 8 cycles and error was calculated as an integral

$$\varepsilon = \int_0^T \left| u(t) - u_{ref}(t) \right| dt \approx \sum \left| u_i - u_{i,ref} \right| \tag{12}$$

where u is the tip displacement and i are the discrete time points corresponding to the case with the longest time step. The case with the shortest time step was used as the reference solution. The error was calculated differently for the beam, because its vibration contains also some vibration modes higher than the 1. mode, which makes comparison of the vibration amplitudes with different time steps difficult.

The error behaviors are plotted in Figure 16. The single d.o.f. case shows approximately 3. order error reduction, whereas for the beam about 2. order behavior is obtained. It is seen that solving the structural dynamics in Abaqus is considerably more accurate than solving the pressure transients in Star-CD, which may have an effect in the coupled CFD-FEM FSI calculations.

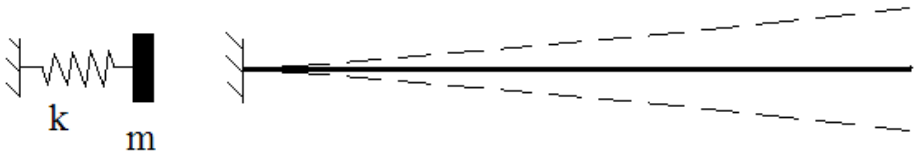

Figure 15. A single d.o.f. oscillator and an oscillating beam.

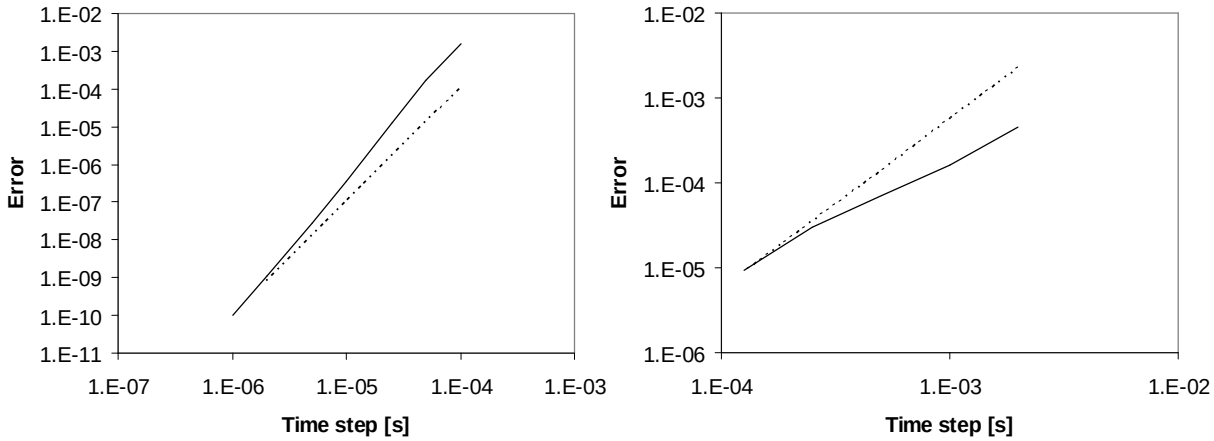

Figure 16. Reduction of error for the single d.o.f. oscillator (left) and for the beam (right). Third (left) and second (right) order slopes are shown with dotted lines.

3.1.3 Piston FSI problem

The one-dimensional piston problem, shown schematically in Figure 17, was used for testing the accuracy of the coupled FSI calculation in a simple case. The length of the cylinder was 1 m with a cross-sectional area of 0.01 m^2. Density ρ_0 = 1000 kg/m^3 and speed of sound c = 1000 m/s were used for the fluid. The piston mass was chosen equal or one tenth of the fluid mass, i.e. m_s = 10 or 1 kg, and the spring stiffness was k = 400 or 40 MN/m. The natural frequency of the pistons without fluid would be

$$f_s = \frac{1}{2\pi}\sqrt{\frac{k}{m_s}} \approx 1007\text{Hz} \qquad (13)$$

The natural frequencies of the systems with incompressible fluid would be

$$f_{s+f} = \frac{1}{2\pi}\sqrt{\frac{k}{m_s + m_f}} \approx 712\text{Hz} \quad \text{or} \quad 303\text{Hz} \qquad (14)$$

The piston had initially a small unbalanced force and was left free to oscillate. Coupling between the Star-CD and Abaqus solutions was achieved by using the explicit coupling of the MpCCI code. Error was calculated from the numerical damping of the oscillation amplitude after a few cycles:

$$\varepsilon = \hat{u}_{ref} - \hat{u}_{calc} \qquad (15)$$

where $\hat{u}_{ref}$ is a reference solution, taken from calculation with the shortest time step.

A problem more relevant to this work would be that of a pressure wave arriving at the fluid-structure interface and thus causing motion of the structure. However, this kind of test case was not calculated as the error in the structural motion would most probably become dominated by the large error of the pressure wave calculation in Star-CD.

Figure 18 shows the piston displacement for the both FSI cases and for the empty pistons. The error behavior is plotted for the FSI cases in Figure 19. The reduction of the error is about 1. order for the both cases.

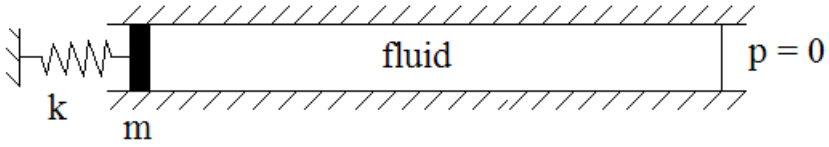

Figure 17. Piston FSI problem.

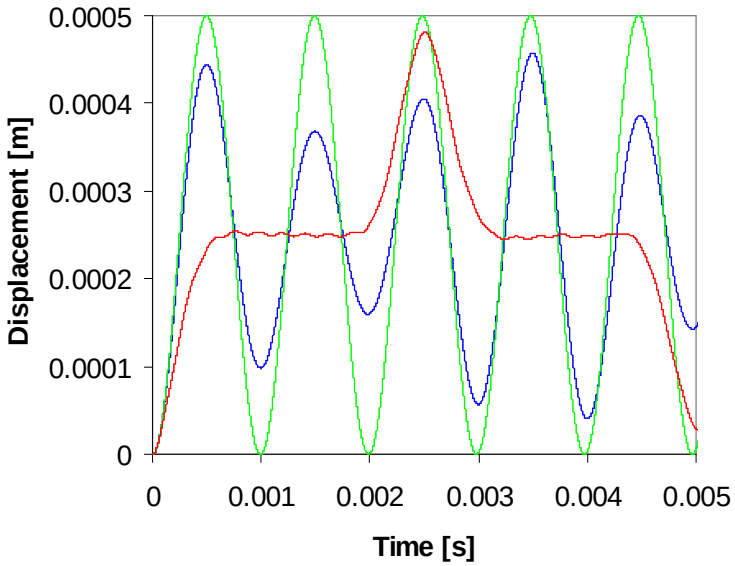

Figure 18. Solutions for the piston FSI problem with $m_s = m_f$ (blue), $m_s = 1/10m_f$ (red) and $m_f = 0$ (green).

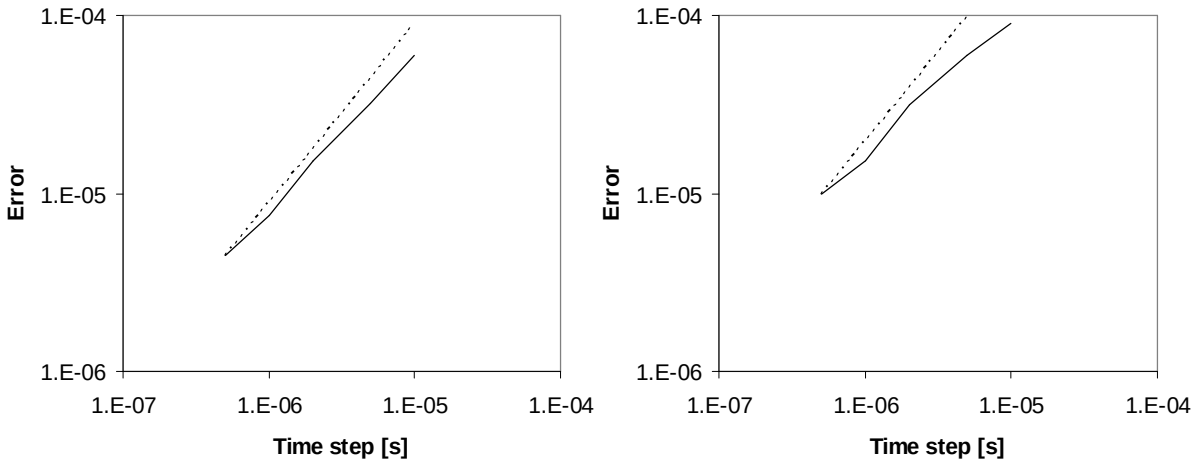

Figure 19. Reduction of error for the piston FSI problem with $m_s = m_f$ (left) and $m_s = 1/10m_f$ (right). First order slope is shown with dotted line.

3.2 Re-run of PPOOLEX experiment SLR-05-02

In the previous calculations by Pättikangas et al. (2010), where the mass flow rate of air was used as boundary condition at the drywell inlet, a delay of about 0.4 s was found in the formation of the first air bubble compared to the experiment. One possible cause for this difference is delay in the mass flow sensor, so that the charging of the drywell with air was possibly in reality faster in the experiment (Puustinen, 2008). In the following, the calculation is re-run by using the measured drywell pressure, shown in Figure 20, as boundary condition at the inlet. Two different meshes, shown in Figure 21, were used. The coarse mesh had about 135 000 hexahedral cells whereas a refined version of this, where the mesh density was doubled in each direction in the pipe and in the bubble area, had about 150 000 cells.

Formation of the first bubble in the pool is shown in Figure 22 for the calculations and experiment. Note that in the plots, times between the calculation and experiment have been synchronized to the moment when the first bubble appears. Using the pressure boundary condition gives somewhat better timing of the bubble formation, but notable delay still exists in the calculation. The refined mesh yields clearly more realistic bubble shape and also the size of the bubbles is slightly closer to the experiment. Also the effect of turbulence modeling and inclusion of surface tension in the calculation were tested, but the effect of these was negligible.

Figure 23 shows pressure at the pool bottom for the calculations with the pressure boundary condition. The pressure rise caused by the initial emptying of the vent pipe is small and similar in magnitude for the both cases. However, approximately after the detachment of the first bubble, quite high pressure oscillations occur which are clearly higher with the finer mesh. These oscillations are perhaps caused by an acoustic mode in the vent pipe, since they are shown clearly also in the pipe but not in the drywell or in the wetwell gas. The oscillations can not be due to bubble dynamics, since the oscillations continue up to about t = 2.7 s with the refined mesh. The calculation with the refined mesh has less numerical damping due to smaller cell size and time step, which explains at least partly the higher amplitude and the longer duration of the oscillations.

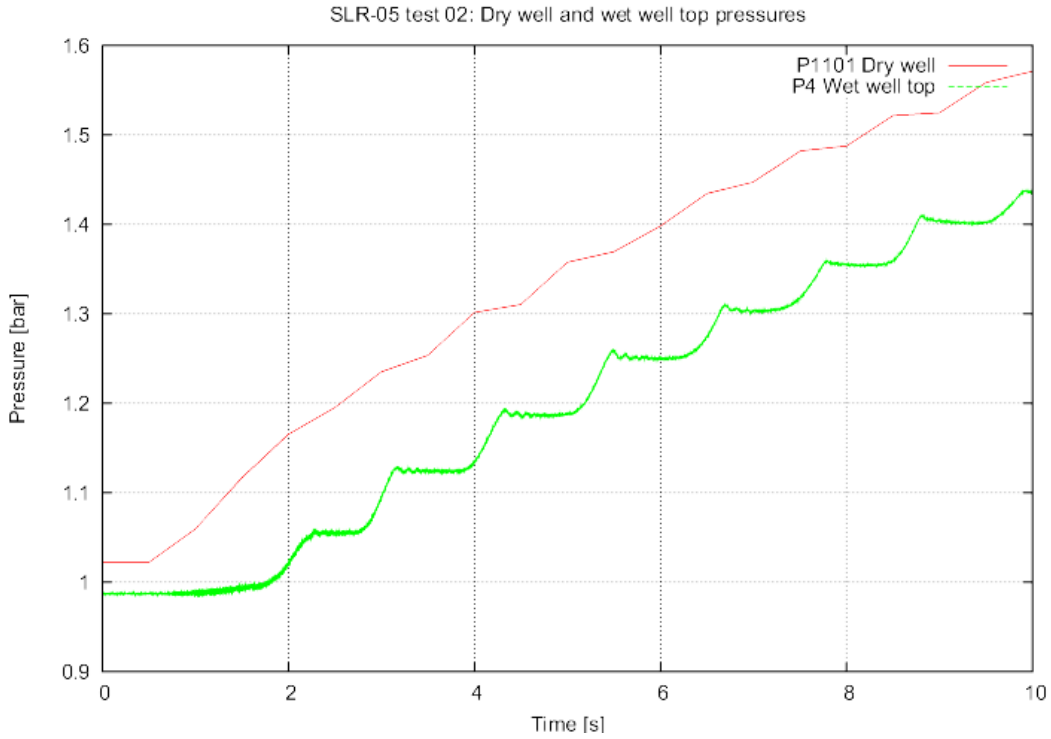

Figure 20. Measured drywell and wetwell pressures in the PPOOLEX experiment SLR-05-02.

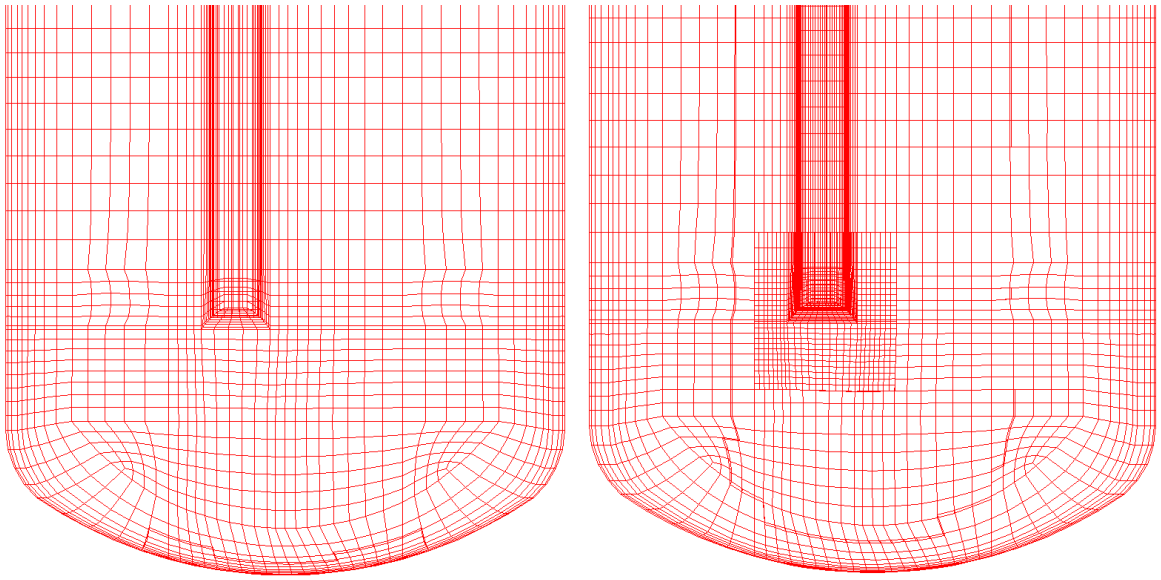

Figure 21. Coarse and refined mesh for the PPOOLEX facility. For the refined mesh, cells were doubled in all directions near the pipe outlet and in the pipe.

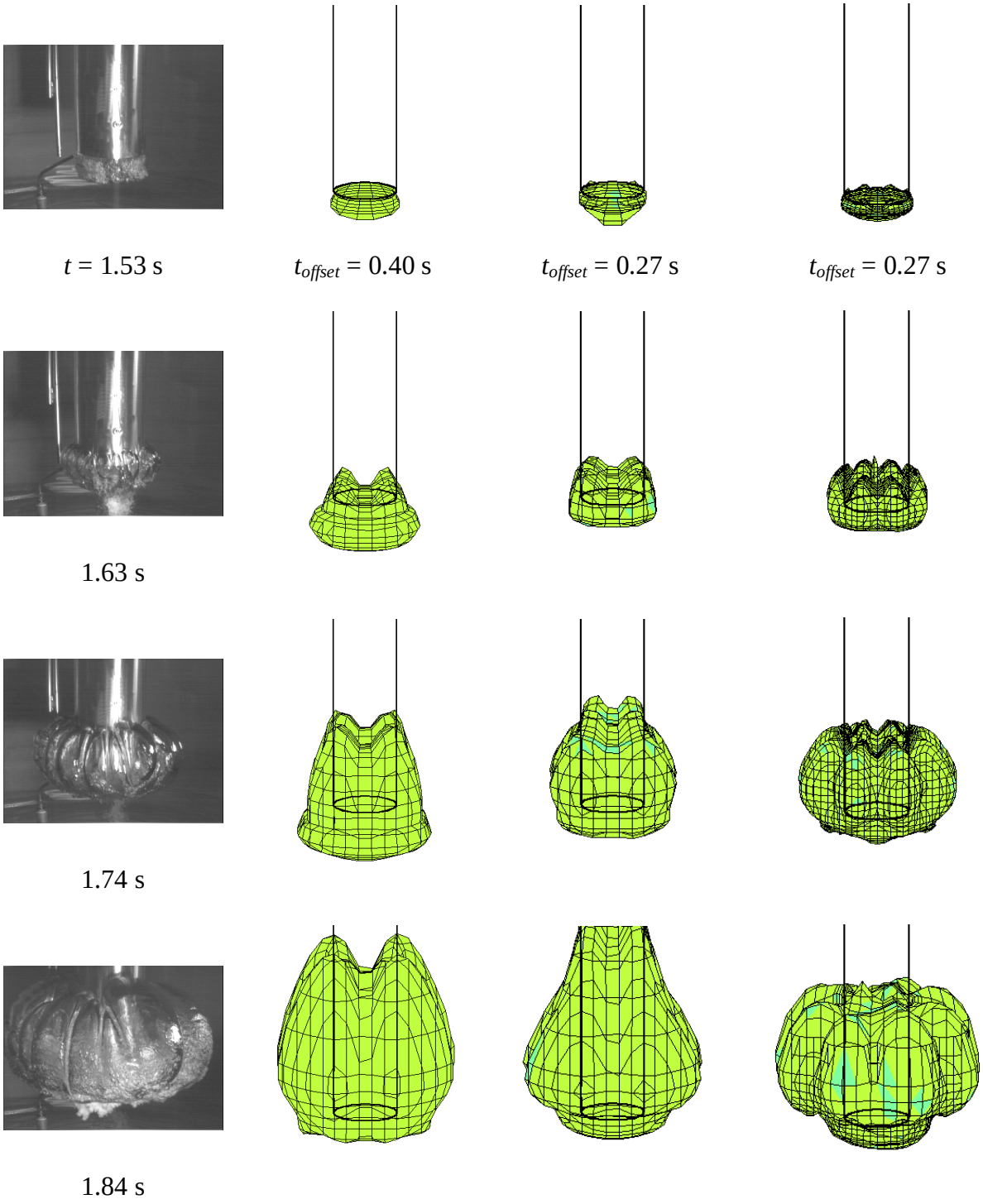

Figure 22. Formation of air bubble at the vent outlet in the PPOOLEX experiment SLR05-02 and in the calculations. Calculated results are shown from left to right for the mass flow BC, pressure BC and pressure BC with refined mesh.

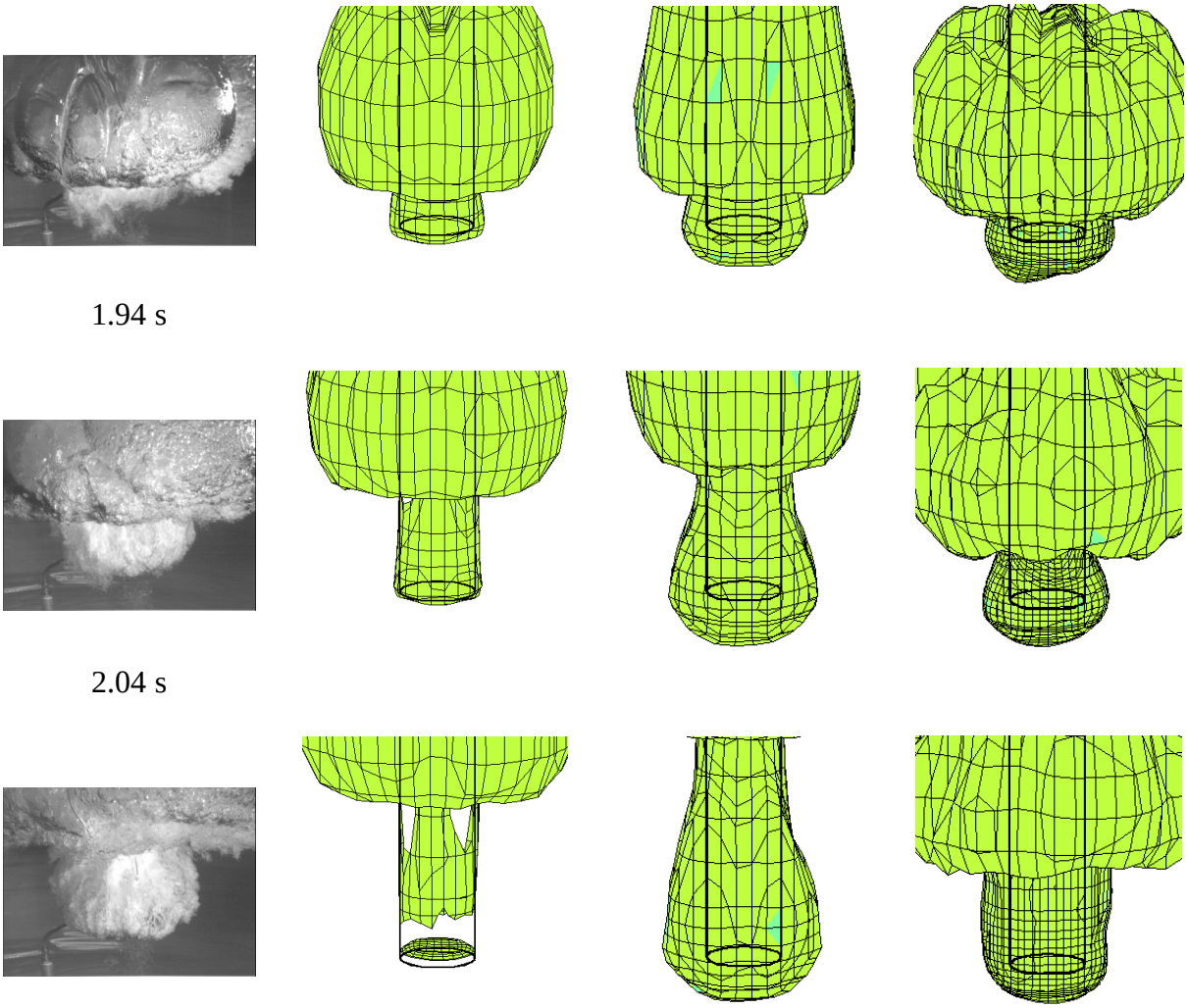

Figure 22. Continues from the previous page.

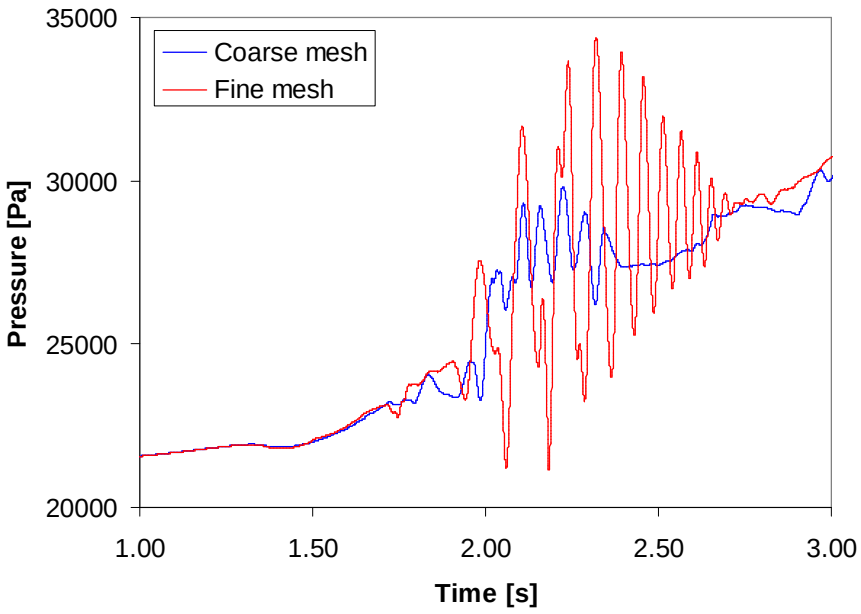

Figure 23. Pressure at the pool bottom for calculations with pressure boundary condition.

3.3 Pressure source due to a collapsing steam bubble

In the following, the collapse of a large steam bubble and the resulting pressure loads are first modeled analytically by using the potential flow theory in a spherically symmetric case. Numerical calculations with Star-CD and Abaqus are then presented and the Abaqus solutions are compared with the analytical ones. The obtained pressure source is used later in Sec. 3.4 in modeling of the BWR containment.

3.3.1 Analytical solutions

3.3.1.1 Pressure field due to a point source

First, we consider the pressure effects of the bubble collapse. Velocity potential for a sole point source in incompressible fluid is (Moody, 1990)

$$\phi(r) = -\frac{\dot{V}}{4\pi r} \tag{16}$$

and the unsteady Bernoulli equation is

$$\rho \frac{\partial \phi}{\partial t} + p + \tfrac{1}{2}\rho V^2 + \rho g z = f(t) \tag{17}$$

By using (16) and (17), assuming zero velocity (i.e. point far away from the bubble) and neglecting the gravity term, we obtain pressure field

$$p(r) - p_\infty = -\rho \frac{\partial \phi}{\partial t} = \frac{\rho \ddot{V}}{4\pi r} \tag{18}$$

which states that the pressure load is caused essentially by the volume acceleration. For compressible fluid, a point source in an infinite medium produces pressure field (Moody, 1990)

$$p(r,t) - p_\infty = \frac{1}{r} F(t - \frac{r}{c}) H(t - \frac{r}{c}) \tag{19}$$

where F is arbitrary, twice-differentiable function and H is the Heaviside step function. Eq. (19) states that pressure disturbances generated by the source propagate spherically with the speed of sound away from the source and diminishing with $1/r$. If the source has an arbitrary volume flow rate $\dot{V}(t)$, the pressure field becomes (Moody, 1990)

$$p(r,t) - p_\infty = \frac{\rho}{4\pi r} \dot{V}'(t - \frac{r}{c}) H(t - \frac{r}{c}) \tag{20}$$

where the prime indicates differentiation with respect to the argument $t - r/c$. The pressure field expressed in terms of volume acceleration is then

$$p(r,t) - p_\infty = \frac{\rho}{4\pi r}\ddot{V}(t - \frac{r}{c})H(t - \frac{r}{c}) \tag{21}$$

3.3.1.2 Collapse with constant bubble pressure

We consider first the simplest case of the bubble collapse, i.e. a spherical bubble having constant pressure in an infinite region of incompressible fluid (Moody, 1990; Pättikangas et al., 2000). The initial bubble radius is R_0, the fluid density is ρ and the pressure difference causing the collapse is $\Delta p_B = p_\infty - p_B$, where p_∞ is pressure far away from the bubble and p_B is pressure inside the bubble. Using the potential flow formulation, an equation of motion for the bubble surface, i.e. the co-called Rayleigh equation for bubble radius, can be derived (Moody, 1990):

$$R\frac{d^2R}{dt^2} + \frac{3}{2}\left(\frac{dR}{dt}\right)^2 = \frac{1}{\rho}[p_B(t) - p_\infty] \tag{22}$$

For a constant under-pressure Δp_B, integration of this equation yields first for the surface velocity

$$\dot{R}(t) = -\left(\frac{2\Delta p_B}{3\rho}\right)^{1/2}\left(\frac{R_0^3}{R(t)^3} - 1\right)^{1/2} \tag{23}$$

The second integration yields the bubble radius as a function of time as

$$t = R_0\left(\frac{\rho}{6\Delta p_B}\right)^{1/2} B(\frac{5}{6},\frac{1}{2})[1 - I_x(\frac{5}{6},\frac{1}{2})] \tag{24}$$

where $B(a,b)$ is the beta function, $I_x(a,b)$ is the incomplete beta function and the normalized bubble volume is $x(t) = (R(t)/R_0)^3$. The total time of the collapse becomes

$$t_{\text{tot}} = 0.9147 R_0\left(\frac{\rho}{\Delta p_B}\right)^{1/2} \tag{25}$$

Acceleration of the bubble surface is according to the equation of motion

$$\ddot{R}(t) = -\frac{1}{R(t)}\left(\frac{\Delta p_B}{\rho} + \frac{3}{2}\dot{R}(t)^2\right) \tag{26}$$

Inserting the velocity (23) into (26) yields a simpler expression

$$\ddot{R}(t) = -\frac{\Delta p_B}{\rho}\frac{R_0^3}{R(t)^4} \tag{27}$$

The bubble radius, surface velocity and surface acceleration are shown in Figure 24 for a bubble in water (ρ = 1000 kg/m^3) with R_0 = 1 m and Δp_B = 1 bar. The surface velocity and acceleration grow infinite as the bubble radius shrinks to zero in about 0.0915 seconds. Here

incompressible fluid was assumed and in reality the fluid compressibility starts to affect the solution roughly when the Mach number Ma = *v/c* becomes larger than 0.3, i.e., *v* > 440 m/s. Also, in reality the small amount of non-condensable gas in the steam starts to limit the bubble shrinking in the late phase of the collapse (see the next section). The finite rate of steam condensation obviously also affects the collapse, but in this work we assume an instantaneous steam condensation for simplicity.

The volume flow rate of the mass sink and the volume acceleration due to the collapsing bubble are obtained by differentiation of the bubble volume with respect to time:

$$V = \tfrac{4}{3}\pi R^3 \tag{28}$$

$$\dot{V} = 4\pi R^2 \dot{R} \tag{29}$$

$$\ddot{V} = 4\pi(R^2\ddot{R} + 2R\dot{R}^2) \tag{30}$$

Inserting the velocity and acceleration of the bubble surface into (30) yields

$$\ddot{V} = \frac{4\pi\Delta p_B}{\rho}\left[-\frac{R_0^3}{R^2} + \frac{4}{3}R\left(\frac{R_0^3}{R^3} - 1\right)\right] \tag{31}$$

Then, in the late phase of the collapse, when $R \to 0$, we have

$$\ddot{V} = \frac{4\pi\Delta p_B R_0^3}{3\rho R^2} = \frac{\Delta p_B V_0}{\rho R^2} \tag{32}$$

The bubble volume and its time derivatives are plotted in Figure 25 according to the values of Figure 24. The volume flow stays bounded and goes to zero in the end. The volume acceleration consists of the “acceleration term” and of the “velocity term”; the both terms grow infinite but have opposite signs. The acceleration term dominates in the early phase whereas the velocity term is larger in the late phase. Consequently, the volume acceleration becomes positive and infinite in the end. The velocity term is interesting in that it is always positive, regardless of the sign of the surface velocity! If the bubble pressure is not constant but grows according to the ideal gas law, the behavior of the acceleration term is somewhat different as is shown in the next section.

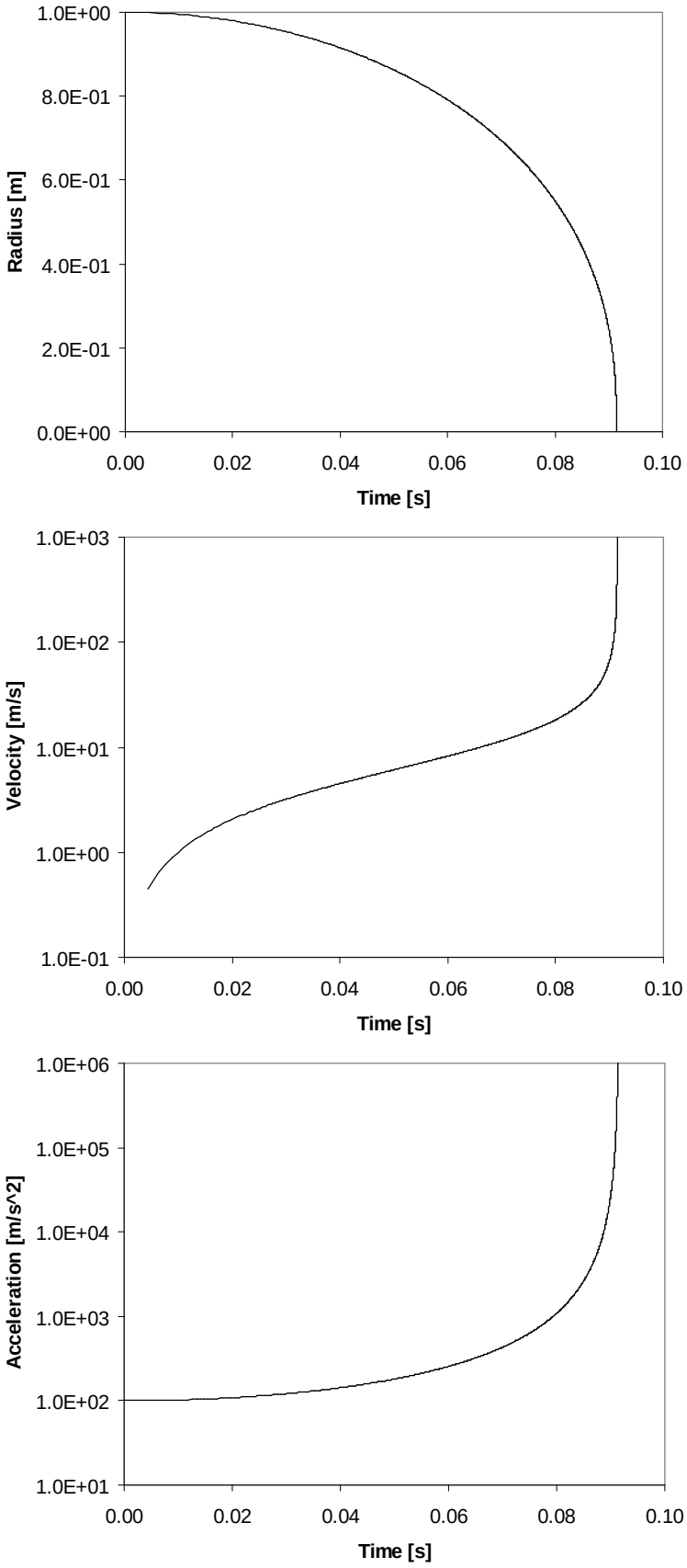

Figure 24. Bubble radius and surface velocity and surface acceleration with constant bubble pressure. Difference between the ambient and bubble pressure is 1 bar.

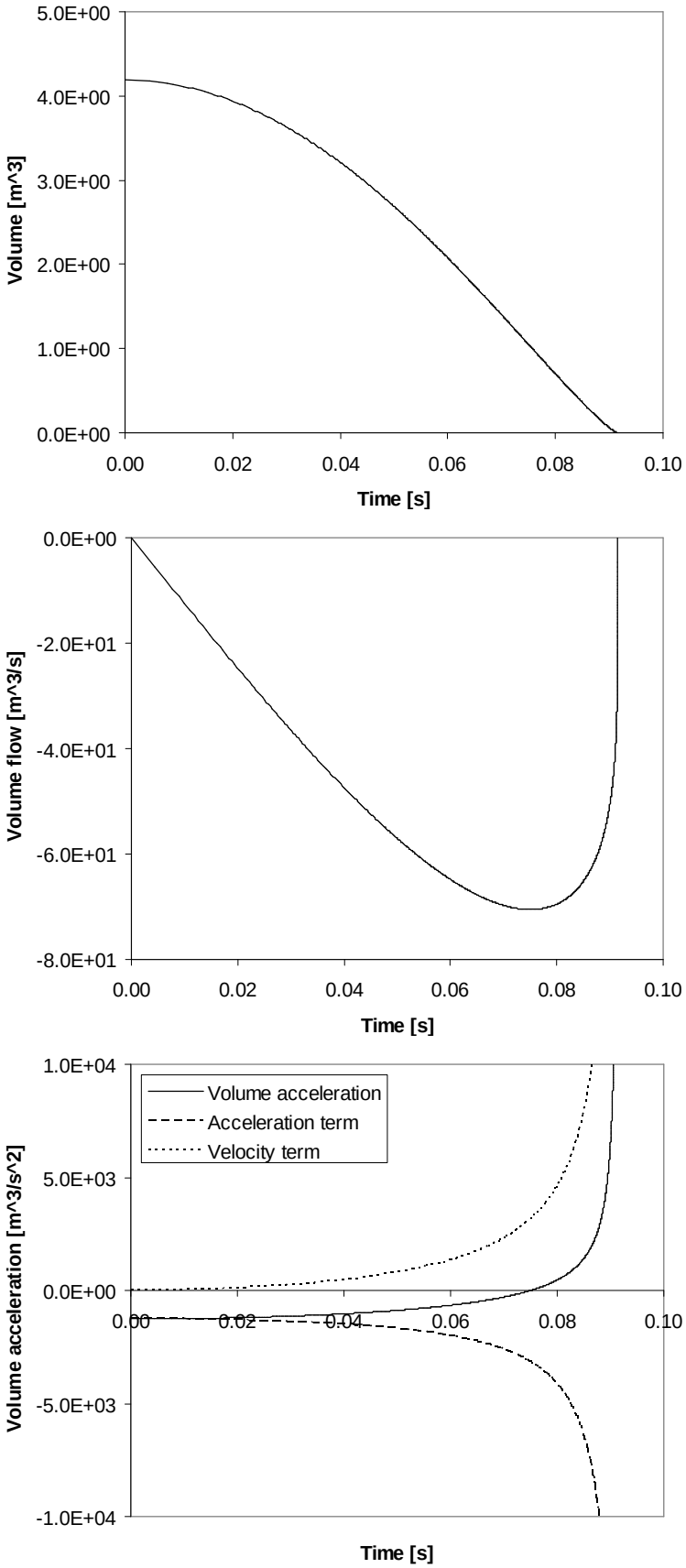

Figure 25. Bubble volume, volume flow and volume acceleration for the bubble collapse of Figure 24.

In the experiments, the bubble has had a toroidal shape rather than spherical due to the presence of the vent pipe. Therefore, it is worth noting here the volume acceleration caused by a collapsing torus. Volume of a torus is

$$V = 2\pi R(\pi r)^2 \tag{33}$$

where R and r are the radii of the torus and of its tube, respectively. In the late phase of the collapse, R may be considered as constant, i.e. equal to the vent pipe radius, and the volume acceleration becomes

$$\ddot{V} = 4\pi^2 R(r\ddot{r} + \dot{r}^2) \tag{34}$$

Thus, if the largest pressure load results from the velocity term as with the spherical bubble, it might be possible to estimate the largest pressure load for the torus directly from the maximum water velocity because the velocity term does not include the tube radius r at all.

3.3.1.3 Collapse of an ideal gas bubble

Next, we consider the case where the bubble has some amount of non-condensable gas in it, so that pressure inside the bubble increases as it gets smaller. Here it is assumed that all of the steam has condensed instantaneously leaving in the bubble only the small amount of non-condensable gas which was among the steam. In the experiments (Puustinen, 2006), even small amounts of air among the steam have suppressed the water-hammer loads. The damping of the pressure pulses was quite strong even with mass fractions of 1 %. Therefore, the main interest in this work is in situations where the mass fraction of air is in the range of 0 … 1 %. Assuming total pressure of 1 bar, this corresponds to partial pressures of air in the range of 0 … 623 Pa.

In the following, water is again assumed as incompressible. We start from an energy balance principle, namely that the kinetic energy of the system must be equal to the work done on the system minus work done on the bubble:

$$E_{kin} = W - W_B \tag{35}$$

The gas is light compared to water and hence the kinetic energy of the gas may be neglected (this assumption can be easily verified afterwards when we have the solution). The kinetic energy of the system is then

$$E_{kin}(R) = \int_R^\infty 2\pi\rho u(r)^2 r^2 dr \tag{36}$$

The fluid velocity field is obtained from the velocity potential (16) as

$$u(r) = \frac{\partial\phi}{\partial r} = \frac{\dot{V}}{4\pi r^2} \tag{37}$$

Inserting this into (36) and performing the integration gives the kinetic energy as a function of the bubble radius:

$$E_{kin}(R) = \frac{\rho \dot{V}^2}{8\pi R} \tag{38}$$

The work done on the bubble is

$$W_B(R) = -\int_{R_0}^{R} 4\pi R^2 p(R) dR \tag{39}$$

The bubble pressure $p(R)$ is derived by using the ideal gas law and the relation for adiabatic reversible compression (Wiksten, 1993):

$$\frac{T_0}{T} = \left(\frac{p_0}{p}\right)^{\frac{\gamma-1}{\gamma}} = \left(\frac{V}{V_0}\right)^{\gamma-1} \tag{40}$$

where γ is the ratio of specific heats and the subscripts 0 denote initial values. Inserting the bubble pressure into (39) and performing the integration, an expression for $W_B(R)$ is obtained. More simply, we can use directly the work of an adiabatic reversible process given by Wiksten (1993):

$$W_B(R) = c_v m[T(R) - T_0] \tag{41}$$

where c_v is the specific heat at constant volume and $T(R)$ is obtained from (40). Because pressure far away from the bubble is constant p_∞, the work done on the system is simply

$$W(R) = p_\infty \Delta V = p_\infty [V_0 - V(R)] \tag{42}$$

The volume flow rate can now be solved as a function of the bubble radius by using (35) and (38):

$$\dot{V}(R) = -\sqrt{\frac{8\pi R}{\rho}[W(R) - W_B(R)]} \tag{43}$$

From (37), the bubble surface velocity becomes

$$\dot{R}(R) = \frac{\dot{V}(R)}{4\pi R^2} \tag{45}$$

Here we don't have the bubble radius as a function of time, because we used the energy balance principle rather than solving a momentum equation as for the constant pressure bubble. However, $R(t)$, $\dot{R}(t)$ and $\ddot{R}(t)$ can be easily determined from $\dot{R}(R)$ by numerical integration and differentiation. The above analytical solutions are compared with numerical ones in Sec. 3.3.3.

It should be noted that the assumptions of ideal gas and of constant value of the ratio of specific heats become questionable in the late phase of the collapse if the amount of non-

condensable gas in the bubble is small, as in this work. This is because the gas pressure and temperature get extremely high values in the late phase.

3.3.2 CFD calculation with Star-CD

Numerical calculations of the rapid collapse of a spherical bubble in an infinite fluid were first performed with Star-CD by using the Volume-Of-Fluid (VOF) model and compressible fluids. The ideal gas law was used for air and a logarithmic equation of state was used for water. Pressure in the gas phase was initialized to a low value which corresponds to the partial pressure of non-condensable gas among the steam. The calculations were run on one- and three-dimensional meshes shown in Figure 26.

The CFD calculation has the advantage that with it the effects of the vent pipe and the pool geometry on the bubble collapse could be accounted for. The results with Star-CD were somewhat promising, but anomalous temperatures were obtained for the air phase. Therefore, different codes or newer versions of Star-CD could be tested in future work. The calculations on one- and three-dimensional meshes gave similar results, which indicates that this kind of calculation method is applicable to three-dimensional cases. The results were found, however, quite sensitive to mesh density and time step.

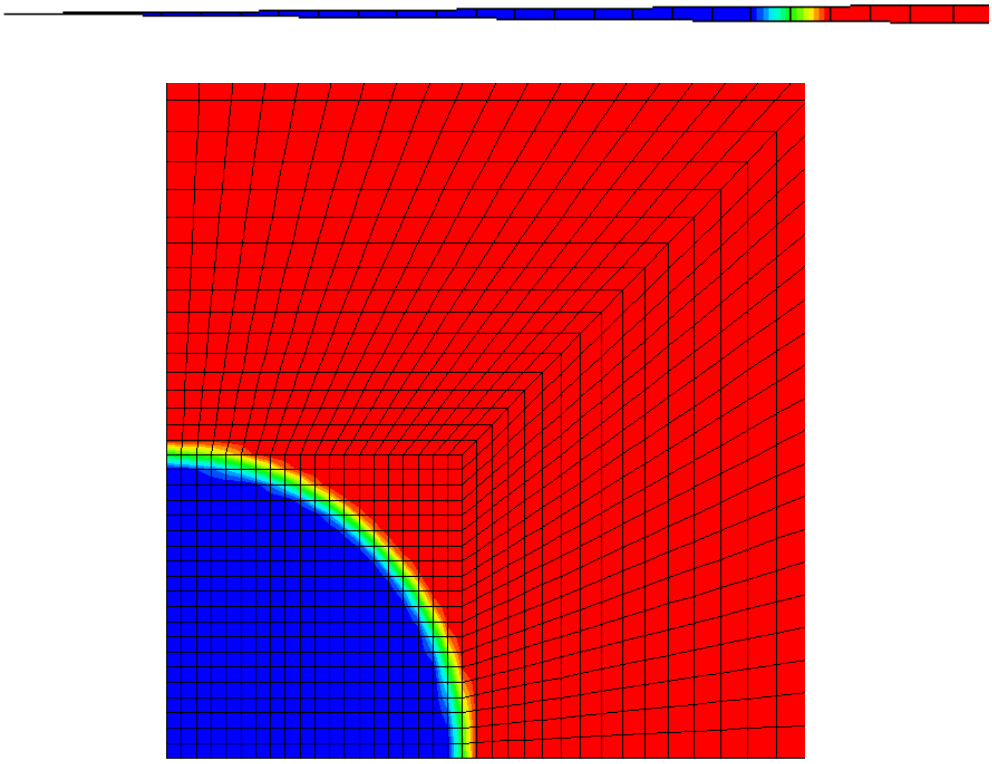

Figure 26. One- and three-dimensional meshes near the bubble and the initial volume fractions of water.

3.3.3 FEM calculation with Abaqus

The bubble collapse was modeled with Abaqus by using stress-displacement elements and fluid equation of states for the gas and water. The ideal gas law was employed for gas and the linear U_s - U_p model for water. Explicit time integration was used and the runs were

geometrically non-linear to account for the large displacements that occur near the bubble. As the fluid velocity grows very high near the bubble, it was found necessary to use adaptive meshing that aims to preserve the original mesh grading near the bubble. Otherwise, the first water element adjacent to the bubble surface became overly stretched in the late phase which affected the results.

Spherical symmetry was assumed so that the model was a narrow slice consisting of a single layer of three-dimensional elements. The mesh of the model is shown in Figure 27 and Figure 28. It was found appropriate to model the air bubble with only one element, since we need to account for only its quasi-static pressure behavior. The total number of elements was about 600. For water, values ρ = 1000 kg/m^3 and c = 1000 m/s were adopted for density and speed of sound, respectively.

The FEM solutions are first compared with the analytical one in Figure 29 – Figure 31 for the case where the bubble has no air in it, i.e. the bubble pressure is constant. In the plots a case, where the speed of sound in water has been increased to 5000 m/s, has been included for comparison since in the analytical solution we assumed incompressible water, i.e. infinite speed of sound. It is seen that the FEM solutions correspond quite well to the analytical one. Also the case without mesh adaptation is accurate except for the very late phase, where the first water element becomes overly stretched. The bubble surface velocity is plotted as a function of the bubble radius in Figure 31; it is seen that the finite speed of sound in the FEM solutions starts to limit the velocity whereas in the analytical solution the velocity grows without bounds.

Results for the case where the bubble pressure is determined from to the ideal gas law are shown in Figure 32 and Figure 33 for initial bubble pressure of 5000 Pa. For comparing the analytical and numerical solutions, a large initial bubble pressure was chosen so that the water velocity stays well below the speed of sound. It is seen that the results are in quite good agreement, although the analytical solution yields somewhat higher maximum velocity. This discrepancy is not caused by the bubble pressure for which the two solutions give practically identical results. One possible cause may be that in the analytical solution the external work done on the system is converted (partly) to the kinetic energy of the water, whereas in the FEM solution it is the initial strain energy in the water which is converted into the fluid motion.

Volume acceleration obtained from the FEM solution is shown in Figure 34 for initial bubble pressure of 500 Pa. The highest values are caused by the velocity term in Eq. (30): the first peak occurs when the bubble radius is decreasing at high velocity whereas the second occurs after the bubble surface “bounces” back and the radius starts to increase. The acceleration term obtains its peak value when the radius obtains its minimum value, i.e. when the velocity is zero. The fact that the highest volume acceleration is caused by the velocity term is somewhat contrary to intuition. Namely, one could easily think that the highest value is caused by the rapid deceleration of the bubble surface velocity at the end of the collapse.

Figure 35 and Figure 36 show the effect of the bubble initial pressure on the results for the analytical and numerical case. Obviously, as the amount of gas in the bubble is decreased, the peak volume acceleration and the peak surface velocity increase. The increase is, however, modest in the numerical solution where the finite speed of sound becomes a limiting factor. These results clearly indicate that the finite speed of sound should be accounted for in modeling the bubble collapse in the condensation pools, since the amount of non-condensable gas in the steam is small.

Figure 37 and Figure 38 show the effect of the initial bubble radius on the results for initial bubble pressure of 500 Pa. Again, the analytical solution yields higher peak values due to the assumption of incompressibility. For both solutions, the peak volume acceleration increases linearly with the initial bubble radius, whereas the peak velocity is unaffected by the initial radius.

Figure 27. Overall mesh of the 1D FEM model.

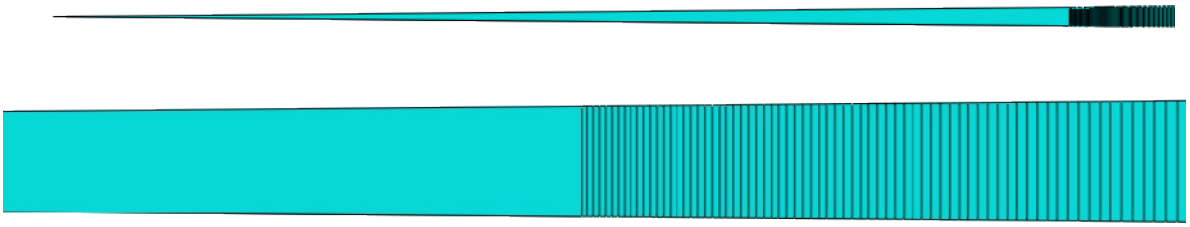

Figure 28. Details of the 1D FEM mesh near the bubble and near the bubble surface.

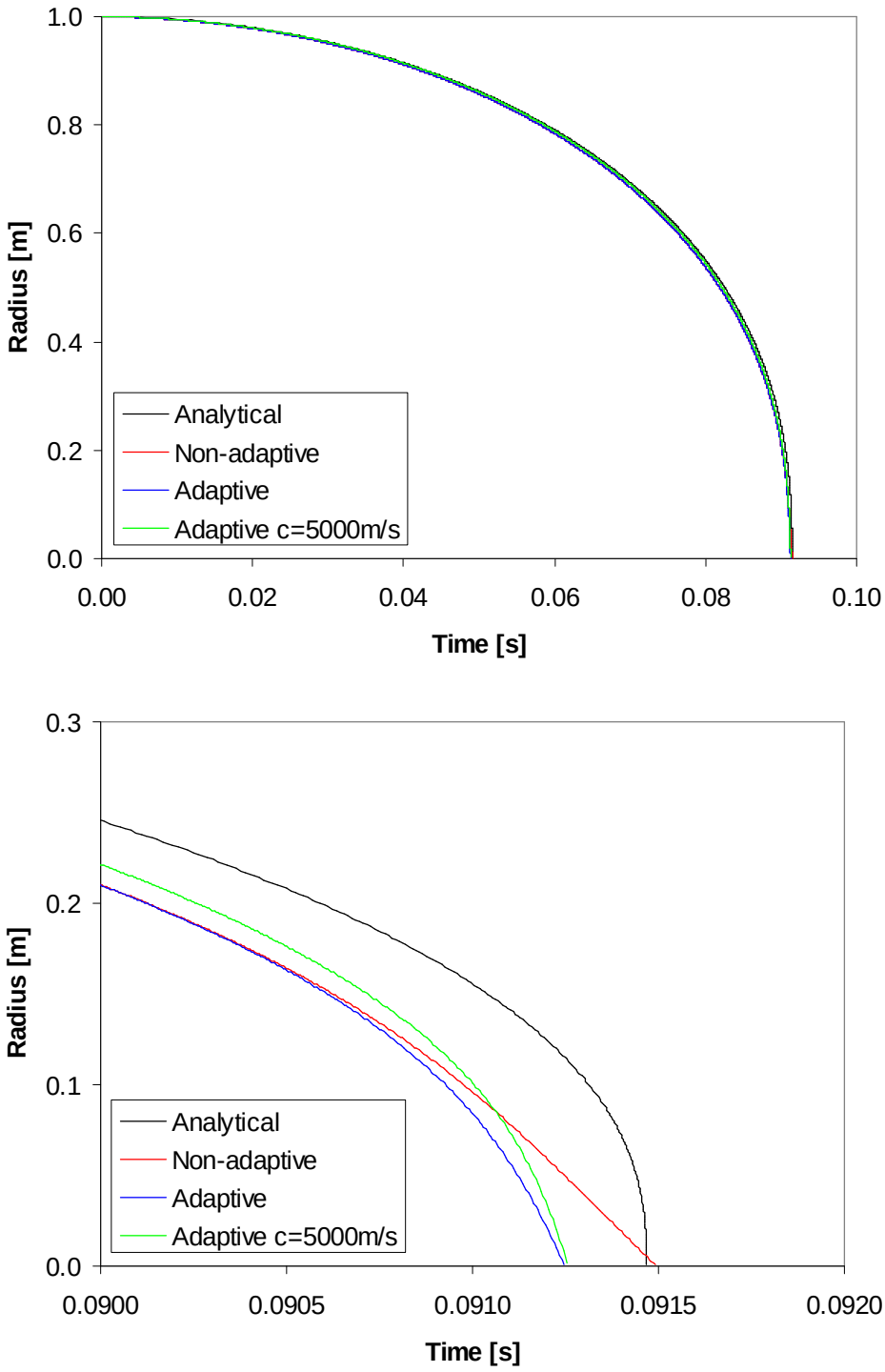

Figure 29. Bubble radius as a function of time with constant bubble pressure.

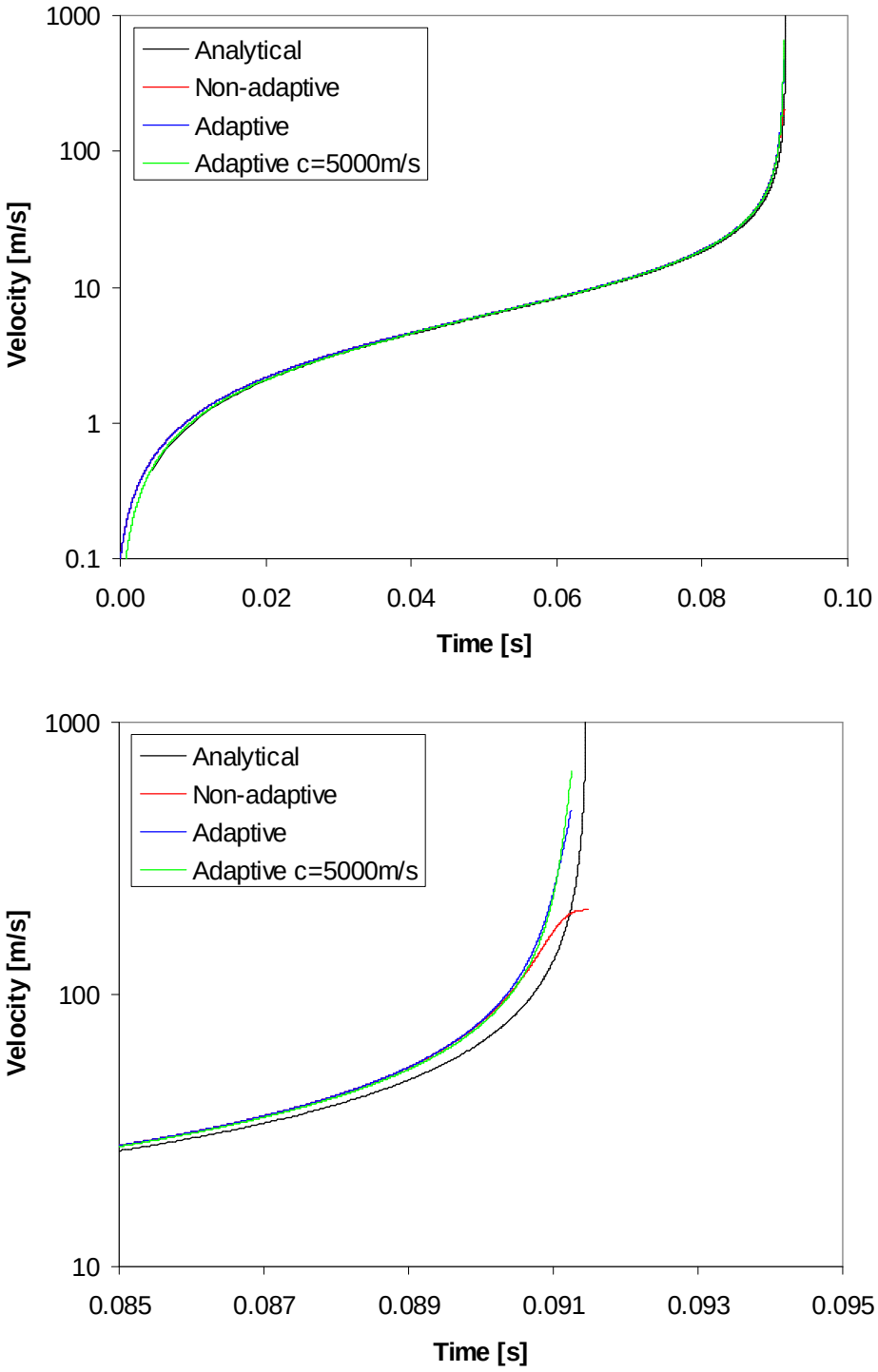

Figure 30. Bubble surface velocity as a function of time with constant bubble pressure.

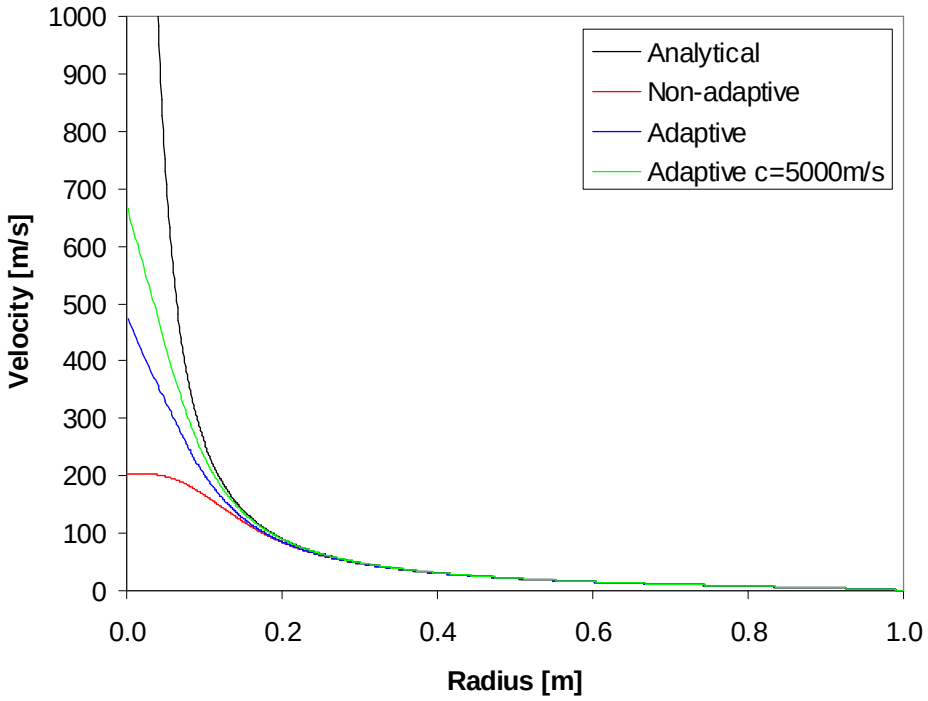

Figure 31. Bubble surface velocity as a function of radius with constant bubble pressure.

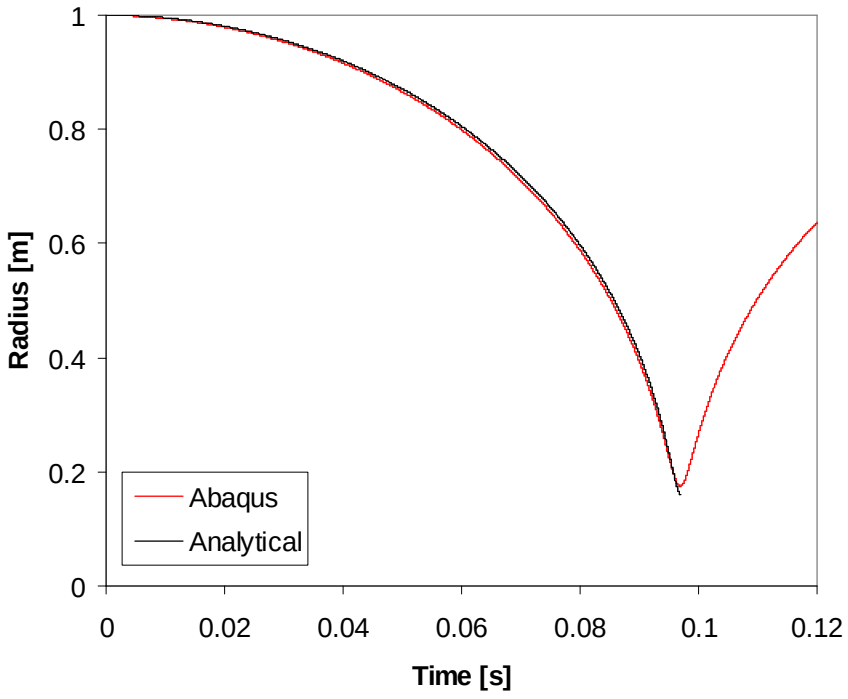

Figure 32. Bubble radius for an ideal gas bubble. The initial bubble pressure is 5000 Pa and the ambient pressure is 1 bar.

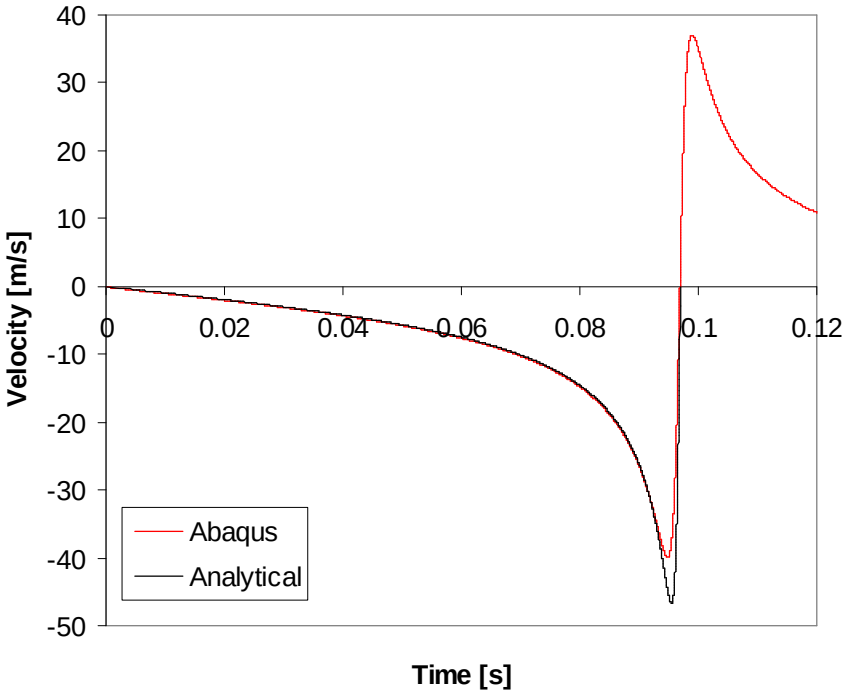

Figure 33. Bubble surface velocity for an ideal gas bubble. The initial bubble pressure is 5000 Pa and the ambient pressure is 1 bar.

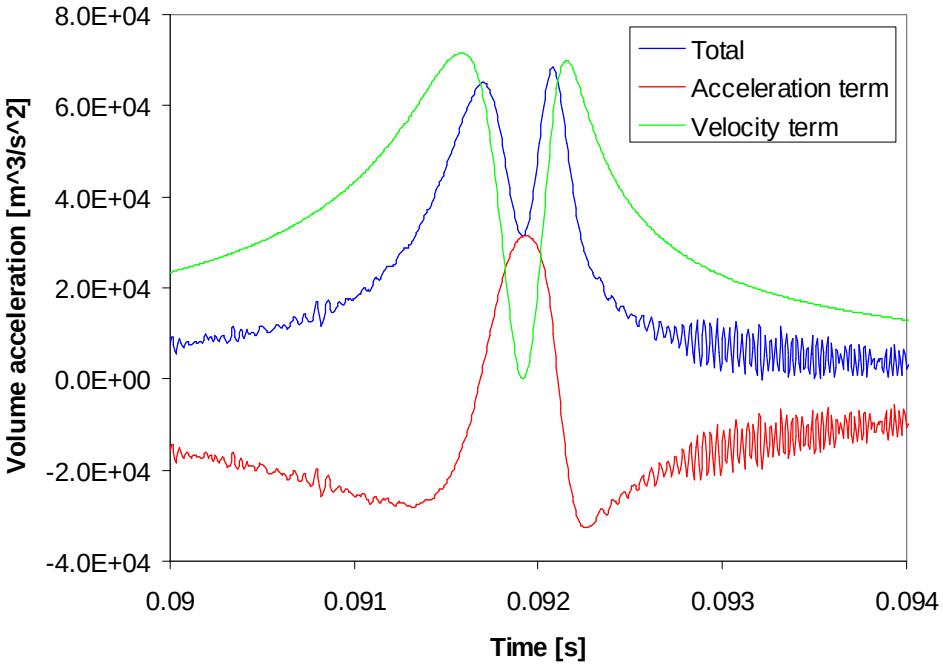

Figure 34. Volume acceleration for an ideal gas bubble. The initial bubble pressure is 500 Pa and the ambient pressure is 1 bar.

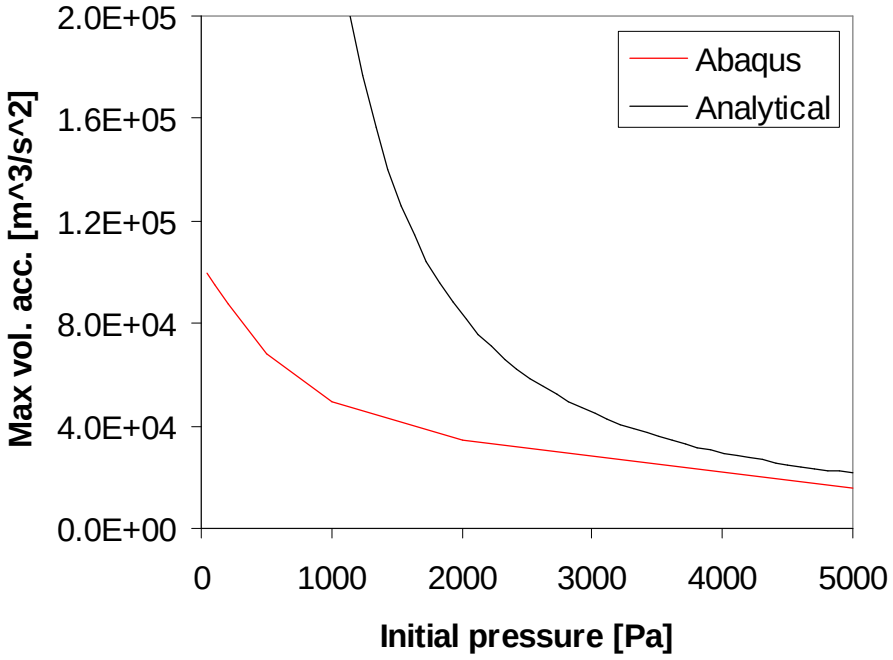

Figure 35. Effect of initial bubble pressure on the maximum volume acceleration.

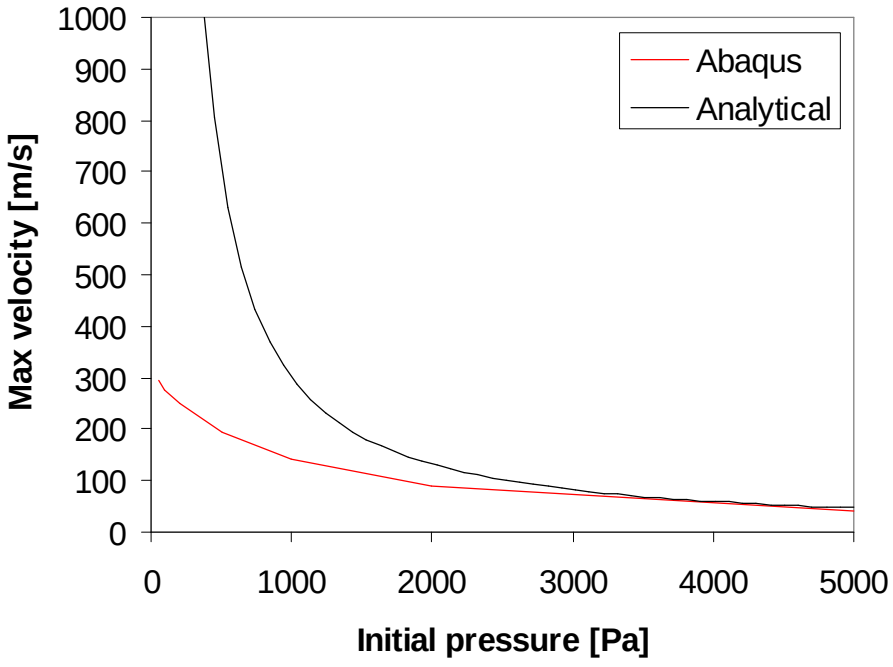

Figure 36. Effect of initial bubble pressure on the maximum bubble surface velocity.

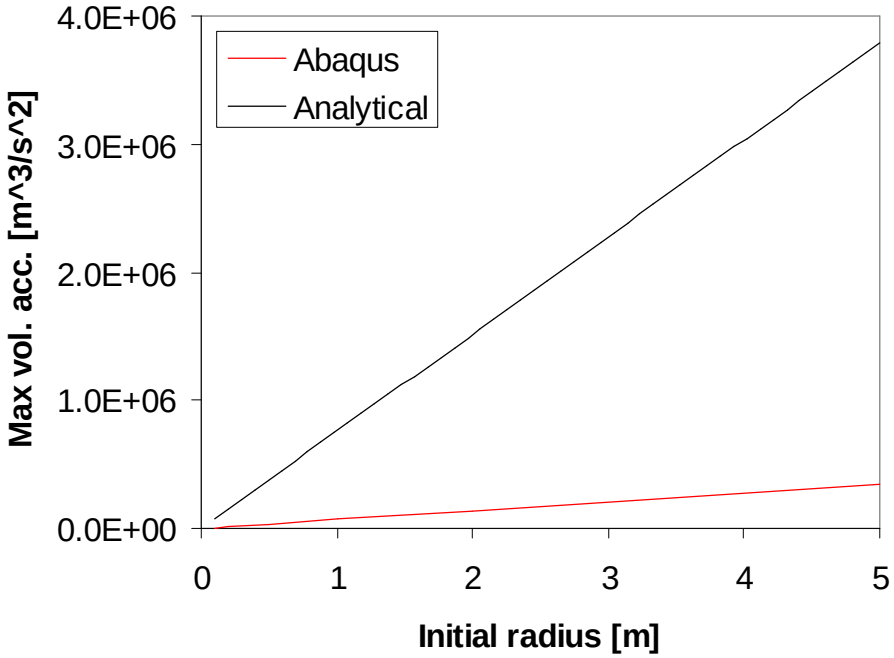

Figure 37. Effect of initial bubble radius on the maximum volume acceleration.

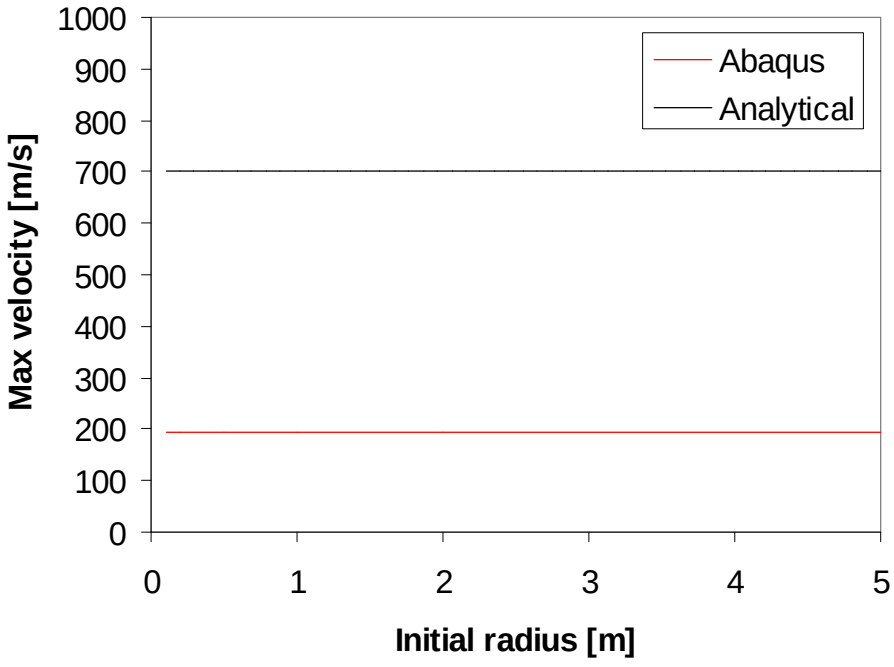

Figure 38. Effect of initial bubble radius on the maximum bubble surface velocity.

3.4 Modeling of a realistic BWR containment

Calculations of the bubble collapse in a BWR containment are presented in the following by using a CFD model and on the other hand an acoustic-structural FEM model. One sixteenth, i.e. 22.5°, sector models of the containment including one vent pipe are used.

3.4.1 CFD calculation

The CFD model had about 170 000 cells and is shown in Figure 39. The VOF model was used for the free surface and the k-ε model for modeling turbulence. The ideal gas law and a logarithmic equation of state suitable for compressible liquid were assumed for air and water, respectively. Time step was 10 µs which results in a maximum sound speed Courant number ($CFL_c = c\Delta t/\Delta x$) of about 0.4.

The initial bubble diameter was 2.4 m, i.e. four times the diameter of the vent pipe. The initial air pressure was set to 500 Pa and pressure in the water was initialized according to the hydrostatic state.

The bubble collapse is shown at the mid-plane of the model in Figure 40. The resulting wall pressure load is plotted in Figure 41. The results seem qualitatively quite correct. If the initial bubble location is raised slightly, a torus-shaped bubble is found at the pipe outlet as in the experiments. The resulting wall pressure is quite significant, as indicated by the structural calculations presented in the next section.

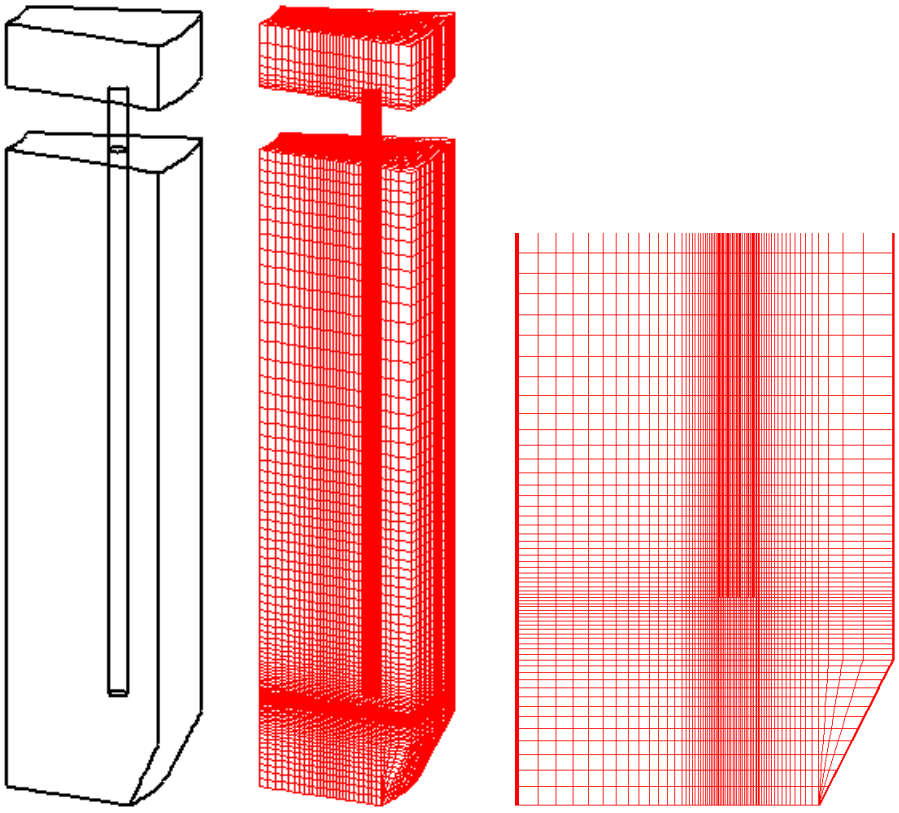

Figure 39. CFD geometry and mesh of the BWR containment.

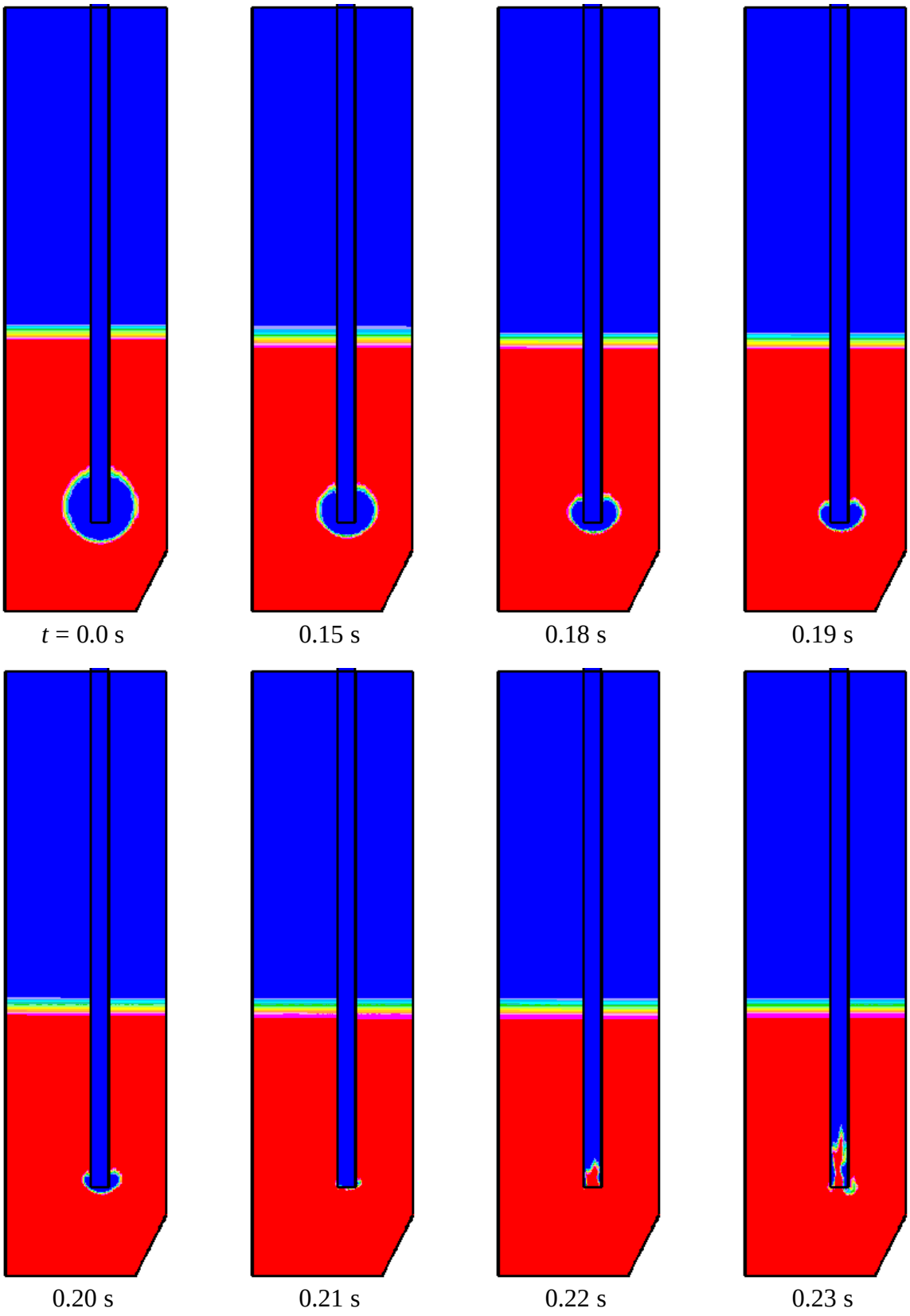

Figure 40. Collapse of a bubble in a BWR containment calculated with the VOF model.

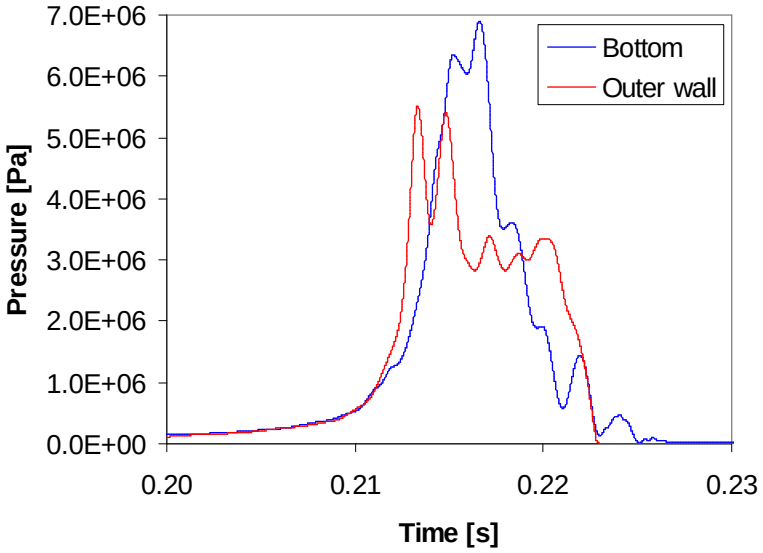

Figure 41. Pressure at the wetwell bottom and at the outer wall at the pipe outlet level for the VOF calculation of the bubble collapse.

From Eq. (25), the bubble collapse time would be about 0.087 s. It is seen that in the calculation the collapse time is more than twice this. The main reason for this is probably the finite pool size which hinders the collapse, i.e. the water sucked in by the collapse can not be replaced as easily in the finite pool. In this particular case, the pool shape is quite slender and the bubble size is significant compared to the pool size, which emphasize the effect of the finite geometry. In the one-dimensional Abaqus calculation, where the air and the finite speed of sound are accounted for, the collapse time is close to the analytical value (see the previous section).

3.4.2 Acoustic-structural FEM calculation

The FEM model representing the sector of the BWR containment is shown in Figure 42. Note that the CFD mesh was used for the wetwell water. The model had about 120 000 and 4000 acoustic and structural elements, respectively. Symmetry boundary conditions were applied to the sides and the bottom of the model was fully fixed.

For concrete, material properties E = 39 GPa, ν = 0.17 and ρ = 2400 kg/m^3 were used for elastic modulus, Poisson's ratio and density, respectively. For the steel cover above the reactor pressure vessel, values E = 206 GPa, ν = 0.3 and ρ = 7850 kg/m^3 were used. The damping ratio was set to 5 % and 4 % for the concrete and steel, respectively (Regulatory Guide 1.61, 2007). The Rayleigh damping was used and these damping ratios were adjusted to be exact at frequencies 10 Hz and 150 Hz, which cover the frequency range of interest in this work. For water, values K = 2.224 GPa and ρ = 1000 kg/m^3 were used for bulk modulus and density, respectively, which corresponds to the speed of sound 1491 m/s.

For modeling the pressure load, a large bubble with initial diameter of 2.4 m, i.e. four times that of the vent pipe, and with initial pressure of 500 Pa was considered. The resulting volume acceleration, obtained with Abaqus as described in Sec. 3.3.3, is shown in Figure 43.

The acoustic pressure is shown at the mid-plane in Figure 44. The volume acceleration obtains its peak value at about t = 17 ms, after which a spherical high-amplitude pressure wave starts to propagate towards the walls. The pressure wave reaches the walls in about

2 ms, after which reflections of the wave can be seen. Here also the wall motion of the containment affects the pressure field due to the FSI coupling.

Deformations and stresses in the containment are shown in Figure 45. The pressure wave makes the lower part of the containment walls to bulge which causes quite high tensile stresses in the outer wall and compressive stresses in the inner wall.

Pressure with and without FSI is plotted as a function of time in Figure 46 at the outer wall at the pipe outlet level. Radial displacements are plotted as a function of time in Figure 47 for the inner and outer walls approximately at the level of maximum deformation. The pressure load and deformations become larger with one-way coupling than with two-way coupling, which is a common result in this kind situation. Also, frequency of the structural motion is higher without FSI.

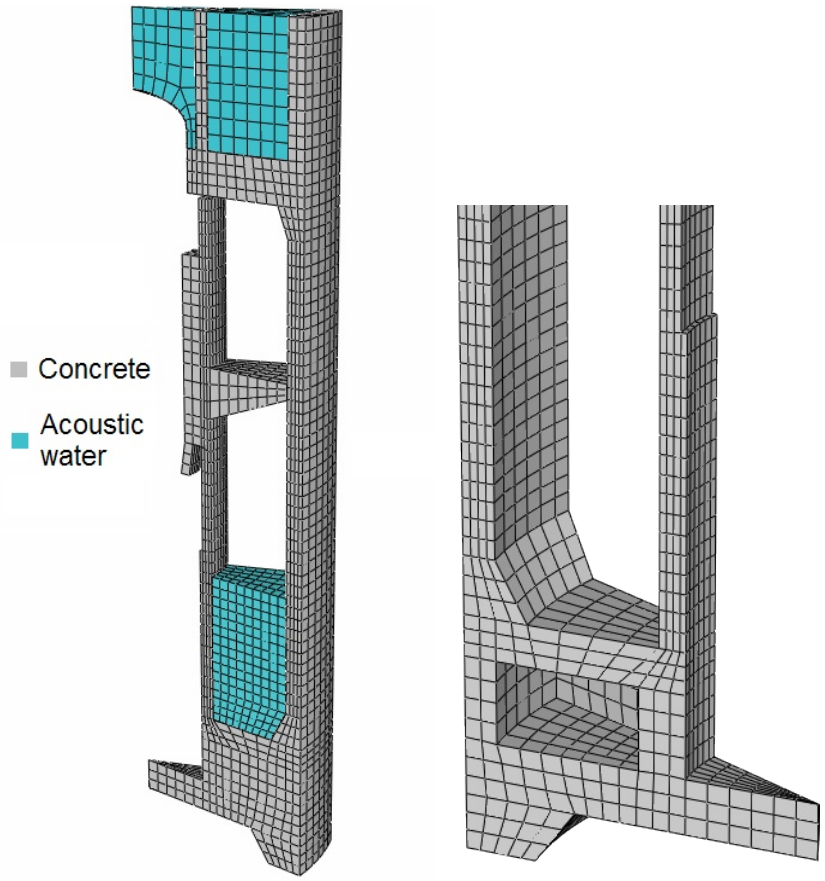

Figure 42. FEM model of the BWR containment. Note that the CFD mesh is used for the wetwell water.

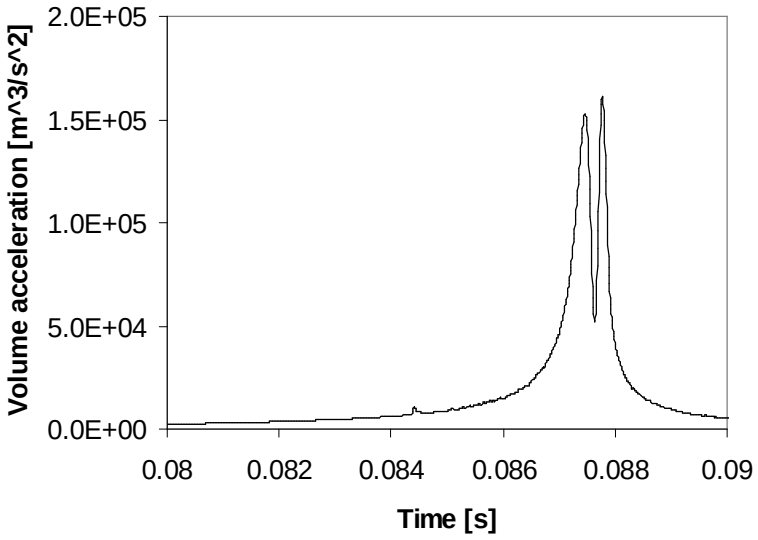

Figure 43. Volume acceleration for bubble with initial radius 1.2 m and initial pressure 500 Pa. Note that the acoustic calculation is started at about t = 71 ms.

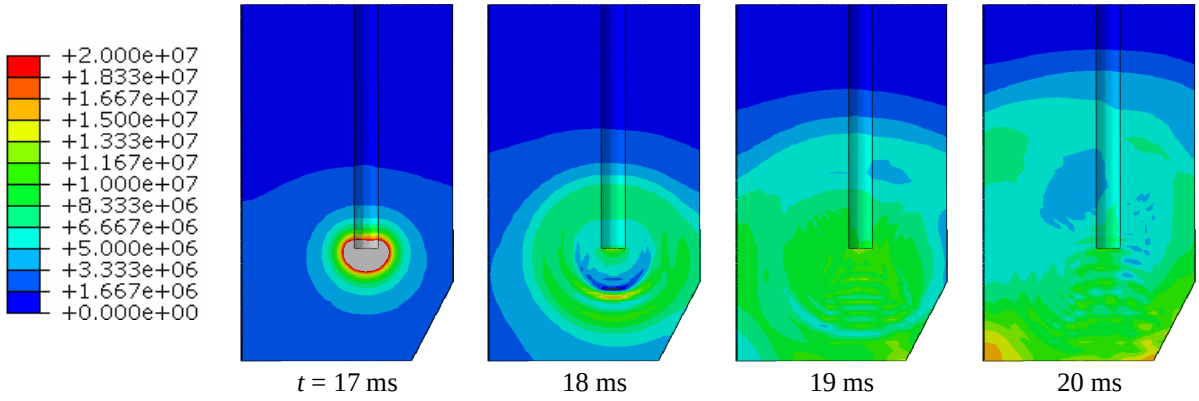

Figure 44. Acoustic pressure [Pa] at the mid-plane of the BWR containment.

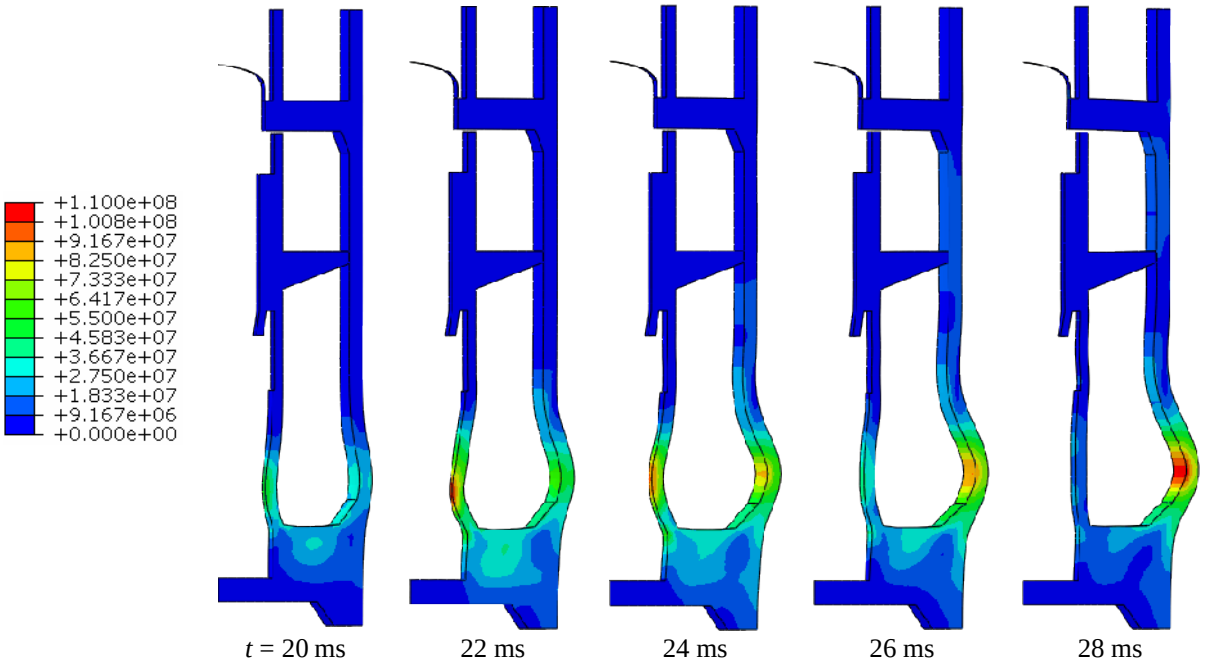

Figure 45. Deformation multiplied by 100 and von Mises stress [Pa] in the BWR containment.

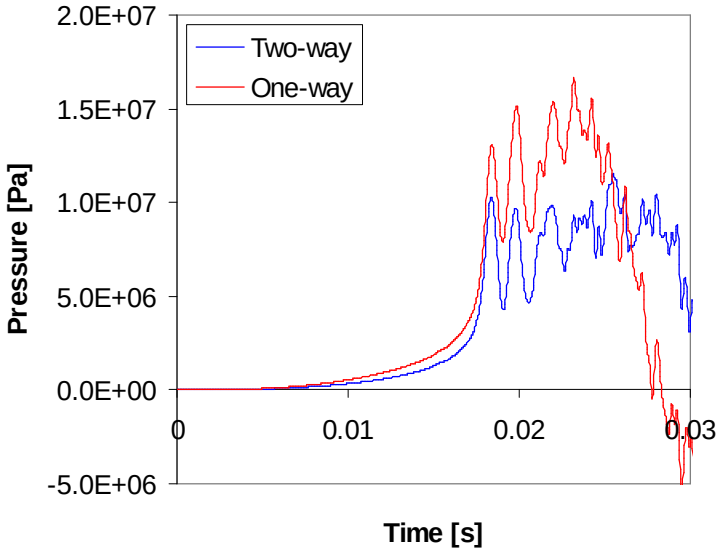

Figure 46. Pressure at the outer wall at the pipe outlet level with one- and two-way FSI.

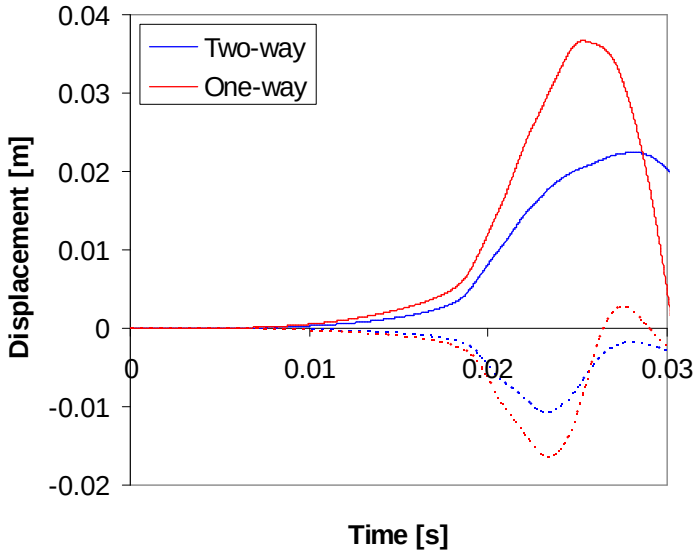

Figure 47. Radial displacements of the outer wall (solid lines) and inner wall (dotted lines) approximately at the level of maximum deformation with one- and two-way FSI.

4 Summary and discussion

Experiments on the behavior of a BWR containment and pressure suppression pool during a hypothetical large-break loss-of-coolant accident are being performed at the Lappeenranta University of Technology. Experiments are performed with the PPOOLEX facility which models the BWR containment having a pressurized drywell compartment and a wetwell with a water pool. In the experiments, vapor is blown from the drywell though vent pipes into the water pool. Recently, interaction of parallel vent pipes has been studied with the PPOOLEX facility by Laine et al. (2009).

In the present work, CFD model for the PPOOLEX facility experiments with parallel vent pipes has been constructed. Two-phase CFD simulations of the experiment PAR-10 have been performed. The direct contact condensation in the water pool has been studied in detail.

The wall condensation and the direct contact condensation were modeled with user-defined functions implemented in the Fluent 12.1 CFD code. In the direct contact condensation model, the Hughes-Duffey correlation for the heat transfer in the liquid phase was implemented (Hughes and Duffey, 1991). The Hughes-Duffey correlation is based on the surface renewal theory presented earlier by Banerjee (1978). The heat transfer coefficient is proportional to the turbulence velocity scale, which is determined by the turbulence kinetic energy on the fluid side: $u_t = C_\mu \sqrt{k_L}$. Turbulent eddies determine the transfer rate of cold water to the interface between the phases.

The Hughes-Duffey correlation was found to produce clearly higher heat transfer coefficients compared to our earlier simulation (Pättikangas et al., 2010b), where the Chen-Mayinger correlation was used. In earlier simulations, incomplete condensation in the water pool occurred, which contradicted the experimental observations.

In the present simulations of the experiment PAR-10, the amount of direct contact condensation obtained in the simulation was in agreement with the experiment. The condensation occurred, however, partly in the rising bubble plumes above the vent outlets. Therefore, it can be concluded that the condensation occurring near the vent outlets is still too weak. The condensation model should still be improved via a more detailed comparison of the simulations to the experiments.

In addition to the heat transfer coefficient, the interfacial area between the liquid and gas is of crucial importance in condensation. Better model for the interfacial area would be needed than the simple gradient model used in the present simulations. It is also possible that a finer mesh near the vent outlets would improve the results somewhat.

The rapid collapse of a large steam bubble and the resulting pressure source were studied analytically and numerically. Pressure source obtained from simplified calculations was used for studying the structural effects and FSI in a realistic BWR containment. The collapse results in volume acceleration, which induces pressure loads on the pool walls. In the case of a spherical bubble, the velocity term of the volume acceleration is responsible of the largest pressure load. As the amount of air in the bubble is decreased, the peak pressure increases. However, when the water compressibility is accounted for, the finite speed of sound becomes a limiting factor. The pressure load and stresses became high in preliminary calculations of a BWR containment, but some of the assumptions are considered conservative. An instantaneous steam condensation was assumed, whereas in reality the condensation rate is finite. This may have a particularly large effect in the important final phase of the collapse, where the water velocity is large and the surface area of the bubble is small. Also, an infinite fluid was assumed in the calculation of the bubble collapse, but in reality the finite size of the pool hinders the collapse somewhat. In the experiments, the bubble has had a toroidal shape rather than spherical due to the presence of the vent pipe. It remains to be shown by detailed CFD calculations of the bubble collapse whether the torus-shaped bubble yields a smaller or larger pressure load. Although crude assumptions were needed in these calculations, they may prove useful in validating more realistic CFD calculations in future.

References

Banerjee, S., 1978. A surface renewal model for interfacial heat and mass transfer in transient two-phase flow, International Journal of Multiphase Flow **4**, 571–573.

Coste, P., Pouvreau, J., Laviélle, J. and Boucker, M., 2008. A two-phase CFD approach to the PTS problem evaluated on COSI experiment, Proc. 16th Int. Conf. on Nuclear Engineering ICONE16, Orlando, FL, USA, May 11–15, 2008.

Hughes, E.D., and Duffey, R.B., 1991. Direct contact condensation and momentum transfer in turbulent separated flows. International Journal of Multiphase Flows **17**, 599.

Lahey, R.T., Jr. and Moody, F.J., 1993. The thermal-hydraulics of a boiling water nuclear reactor, 2nd edition, American Nuclear Society, USA.

Laine, J., Puustinen, M. and Räsänen, A., 2009. PPOOLEX experiments with two parallel blowdown pipes, Lappeenranta University of Technology, Nuclear Safety Research Unit, Research Report CONDEX 1/2009, 49 p.

Moody, F.J., 1990. Introduction to unsteady thermofluid mechanics, Wiley, New York.

Puustinen, M., 2006. Combined effects experiments with the condensation pool test facility. Lappeenranta University of Technology, Nuclear Safety Research Unit, Research report POOLEX 1/2006, 30 p. + app. 6 p.

Puustinen, M., 2008. Personal communication.

Puustinen, M., Laine, J. and Räsänen, A., 2010. PPOOLEX experiments on dynamic loading with pressure feedback, Lappeenranta University of Technology, Nuclear Safety Research Unit, Research report CONDEX 2/2009, 42 p.

Pättikangas, T., Raussi, P., Pokela, H. and Huttunen, M., 2000. Two-dimensional CFD simulation of water hammer in a pool. VTT Technical Research Centre of Finland, Research Report ENE6/26/00, Espoo, Finland, 22 p. + app. 4 p.

Pättikangas, T., Niemi, J. and Timperi, A., 2008. Modelling of blowdown of air in the pressurized PPOOLEX facility, VTT Technical Research Centre of Finland, Research Report VTT-R-02233-08, Espoo, Finland, 85 p.

Pättikangas, T., Niemi, J. and Timperi, A., 2010a. CFD and FEM modelling of PPOOLEX experiments. VTT Technical Research Centre of Finland, Research Report VTT-R-02187-10, Espoo, Finland, 39 p.

Pättikangas, T.J.H., Niemi, J., Laine, J., Puustinen, M. and Purhonen, H., 2010b. CFD modelling of condensation of vapour in the pressurised PPOOLEX facility, CFD4NRS-3, Experimental Validation and Application of CFD and CMFD Codes to Nuclear Reactor Safety Issues, OECD/NEA & IAEA Workshop, Washington D.C., USA, 14–16 September, 2010, 12 p.

Regulatory Guide 1.61, 2007. Damping values for seismic design of nuclear power plants. U.S. Nuclear Regulatory Commission.

Štrubelj, L. Ézsöl, G. and Tiselj, I., 2010. Direct contact condensation induced transition from stratified to slug flow, Nuclear Engineering and Design **240**, 266–274.

Tanskanen, V., Lakehal, D. and Puustinen, M., 2008. Validation of direct contact condensation CFD models against condensation pool experiment, Workshop on Experiments and CFD Code Application to Nuclear Reactor Safety (XCFD4NRS), Grenoble, France, 10–12 September, 2008, 12 p.

Wiksten, R., 1993. Lämpövoimaprosessit. Teknillinen korkeakoulu, Energiatekniikan laitos, Otaniemi.

Title	Numerical modelling of pressure suppression pools with CFD and FEM codes
Author(s)	Timo Pättikangas, Jarto Niemi and Antti Timperi
Affiliation(s)	VTT Technical Research Centre of Finland
ISBN	978-87-7893-321-8
Date	June 2011
Project	NKS-R / POOL
No. of pages	53
No. of tables	2
No. of illustrations	47
No. of references	17

Abstract

Experiments on large-break loss-of-coolant accident for BWR is modeled with computational fluid (CFD) dynamics and finite element calculations. In the CFD calculations, the direct-contact condensation in the pressure suppression pool is studied. The heat transfer in the liquid phase is modeled with the Hughes-Duffey correlation based on the surface renewal model. The heat transfer is proportional to the square root of the turbulence kinetic energy. The condensation models are implemented with user-defined functions in the Euler-Euler two-phase model of the Fluent 12.1 CFD code.

The rapid collapse of a large steam bubble and the resulting pressure source is studied analytically and numerically. Pressure source obtained from simplified calculations is used for studying the structural effects and FSI in a realistic BWR containment. The collapse results in volume acceleration, which induces pressure loads on the pool walls. In the case of a spherical bubble, the velocity term of the volume acceleration is responsible of the largest pressure load. As the amount of air in the bubble is decreased, the peak pressure increases. However, when the water compressibility is accounted for, the finite speed of sound becomes a limiting factor.

Key words Condensation pool, pressure suppression pool, BWR, CFD, fluid-structure interactions, FSI

Available on request from the NKS Secretariat, P.O.Box 49, DK-4000 Roskilde, Denmark.
Phone (+45) 4677 4045, fax (+45) 4677 4046, e-mail nks@nks.org, www.nks.org